Aerosol optical properties in a rural environment near the mega-city Guangzhou, China: implications for regional air pollution and radiative forcing

R. M. Garland, H. Yang, O. Schmid, D. Rose, A. Nowak, P. Achtert, A. Wiedensohler, N. Takegawa, K. Kita, Y. Miyazaki, et al.

Atmos. Chem. Phys. Discuss., 8, 6845–6901, 2008
www.atmos-chem-phys-discuss.net/8/6845/2008/

Atmospheric Chemistry and Physics Discussions

Aerosol optical properties in a rural environment near the mega-city Guangzhou, China: implications for regional air pollution and radiative forcing

R. M. Garland[1], H. Yang[1], O. Schmid[2], D. Rose[1], A. Nowak[4], P. Achtert[4], A. Wiedensohler[4], N. Takegawa[5], K. Kita[5], Y. Miyazaki[5], Y. Kondo[5], M. Hu[3], M. Shao[3], L. Zeng[3], Y. Zhang[3], M. O. Andreae[1], and U. Pöschl[1]

[1]Biogeochemistry Department, Max Planck Institute for Chemistry, Mainz, Germany
[2]Helmholtz Center Munich, German Research Center for Environmental Health, Institute for Inhalation Biology, Neuherberg/Munich, Germany
[3]College of Environmental Sciences, Peking University, Beijing, China
[4]Leibniz Institute for Tropospheric Research, Leipzig, Germany
[5]RCAST, University of Tokyo, Tokyo, Japan

Received: 6 February 2008 – Accepted: 10 March 2008 – Published: 9 April 2008

Correspondence to: R. M. Garland (garland@mpch-Mainz.mpg.de)

Published by Copernicus Publications on behalf of the European Geosciences Union.

Abstract

The scattering and absorption of solar radiation by atmospheric aerosols is a key element of the Earth's radiative energy balance and climate. The optical properties of aerosol particles are, however, highly variable and not well characterized, especially near newly emerging mega-cities. In this study, aerosol optical properties were measured at a regional background site approximately 60 km northwest of the mega-city Guangzhou in southeast China. The measurements were part of the "Program of Regional Integrated Experiments of Air Quality over the Pearl River Delta" intensive campaign (PRIDE-PRD2006), covering the period of 1–30 July 2006. Scattering and absorption coefficients of dry aerosol particles with diameters up to 10 μm (PM_{10}) were determined with a three-wavelength integrating nephelometer and with a photoacoustic spectrometer, respectively.

Averaged over the measurement campaign (arithmetic mean ±standard deviation), the total scattering coefficients were 200±133 Mm^{-1} (450 nm), 151±103 Mm^{-1} (550 nm) and 104±72 Mm^{-1} (700 nm) and the absorption coefficient was 34.3±26.5 Mm^{-1} (532 nm). The average Ångström exponent was 1.46±0.21 (450 nm/700 nm) and the average single scattering albedo was 0.82±0.07 (532 nm) with minimum values as low as 0.5. The low single scattering albedo values indicate a high abundance of, as well as strong sources of light absorbing carbon (LAC). The ratio of LAC to CO concentration was highly variable throughout the campaign, indicating a complex mix of different combustion sources. The scattering and absorption coefficients, as well as the Ångström exponent and single scattering albedo, exhibited pronounced diurnal cycles, which can be attributed to boundary layer mixing effects and enhanced nighttime emissions of LAC (diesel soot from regulated truck traffic). The daytime average single scattering albedo of 0.87 appears to be more suitable for climate modeling purposes than the 24-h average of 0.82, as the latter value is strongly influenced by fresh emissions into a shallow nocturnal boundary layer. In spite of high photochemical activity during daytime, we found no evidence for strong

local production of secondary aerosol mass.

The relatively low average mass scattering efficiency with respect to PM_{10} ($2.84 \pm 0.037\,m^2\,g^{1}$, λ=550 nm) indicates a high proportion of mass in the coarse particle fraction (diameter >1 μm). During high pollution episodes, however, the Ångström exponent exhibited a dependence on wavelength, which indicates an enhancement of the fine particle fraction during these periods. A negative correlation between single scattering albedo and backscatter fraction was observed and found to affect the impact that these parameters have on aerosol radiative forcing efficiency.

1 Introduction

Mega-cities, large urban areas with populations of greater than 10 million people, emerged in the twentieth century. In 1950 there were only two (New York and Tokyo) and in 2005 there were twenty (U.N., 2005). While there are many benefits to this increased urbanization (i.e., more access to education and economic advantages), this high growth rate also presents many environmental problems, including the degradation of air quality. The environmental impacts of air pollution in large cities are not just restricted to their borders, but rather the pollutants are transported and can then have regional and global impacts (Lawrence et al., 2007).

Aerosol particles are a major component of urban air pollution and can have negative effects on human health, can impact cloud formation and lifetime and can influence heterogeneous reactions (Seinfeld and Pandis, 1998; Finlayson-Pitts and Pitts, 1999; Poeschl, 2005). Moreover, they scatter and absorb incoming solar radiation impacting visibility as well as the radiative balance of the atmosphere. For example, the increasing concentrations of anthropogenic aerosol particles in China since the 1950's have been linked to decreasing amounts of sunshine duration and changing summertime maximum temperatures (Kaiser and Qian, 2002).

The Pearl River Delta (PRD) region in southeastern China is a rapidly growing area, both economically and in population. This area contains many cities, including Hong

ACPD

8, 6845–6901, 2008

Title Page
Abstract | Introduction
Conclusions | References
Tables | Figures
◄◄ | ►►
◄ | ►
Back | Close
Full Screen / Esc
Printer-friendly Version
Interactive Discussion

Kong, Guangzhou and Shenzhen. The PRD region gets it name from the Pearl River that, together with its tributaries, runs through this region. The river delta is bordered by the Nan Ling Mountains from the northwest to the southwest and the river empties into the South China Sea in between Hong Kong and Macau. Guangdong province, which contains both Guangzhou and Shenzhen, has a population of approximately 92 million people and the third largest Gross Domestic Product in China (NBS, 2007). By 2015, Guangzhou itself is projected to have more than 10 million inhabitants, and will thus be considered a mega-city (U.N., 2005). As the industry in the PRD region increases, so do the environmental impacts of this growth. Nearly half of the urban river water bodies in Guangdong province are seriously polluted; leading to clean water shortages in an area with large natural water resources (Ouyang et al., 2006). The increase in industry and population also impacts the area's air quality.

The PRD region is often plagued with high aerosol concentrations that lead to not only low visibility, but can also impact the radiative balance of the region (Wu, Tie et al., 2005). Previous studies in PRD have measured average aerosol mass concentrations for PM_{10} (particulate matter with aerodynamic particle diameter $\leq$10 μm) of 70–234 $\mu g/m^3$ (Wei et al., 1999; Cao et al., 2003; Cao et al., 2004; Liu et al., 2007), with average concentrations generally above 200 $\mu g/m^3$ in Guangzhou in the winter (Cao et al., 2003) and around 100 $\mu g/m^3$ ($PM_{2.5}$; particulate matter with aerodynamic particle diameter $\leq$2.5 μm) in the fall (Andreae et al., 2008), and with a large percentage of the particulate mass (>58%) in the $PM_{2.5}$ fraction.

Andreae et al. (2008) measured the aerosol optical properties in urban Guangzhou in October 2004 as part of the "Program of Regional Integrated Experiments of Air Quality over the Pearl River Delta" (PRIDE-PRD) campaign 2004. During that campaign the air masses generally came from the northeast, bringing continental pollution into the PRD region (Gnauk, et al., 2008[1]). In contrast, this current study characterizes the

[1]Gnauk, T., Mueller, K., van Pinxteren, D., He, L. Y., Niu, Y., Hu, M., and Herrmann, H.: Size-segregated particulate chemical composition in Xinken, Pearl River Delta, China: OC/EC and organic compounds, Atmos. Environ., submitted, 2008.

properties of aerosols and regional pollution from sources in the Pearl River Delta itself. During the PRIDE-PRD2006 campaign in July 2006, we measured the aerosol optical properties in a regional background site ∼60 km NW of the city of Guangzhou. As a result of the monsoon circulation, the sampled air masses came mainly from the south/southeast, off the South China Sea and passing over the PRD region before arriving at the measurement site.

2 Methods

2.1 Measurement location and supporting data

The measurements were performed in Backgarden (23.548056° N, 113.066389° E), a small village in a rural environment at the outskirts of the densely populated center of the PRD (Fig. 1). A two-story hotel located next to a reservoir was used exclusively to house the measurement campaign, with most of the instruments placed in air conditioned rooms on the top floor and sample inlets mounted on the rooftop.

Local meteorological parameters were measured on the roof, next to the sample inlets (Weather Transmitter WXT510, Vaisala, Finland; operated by University of Tokyo). The average meteorological values (arithmetic mean ± standard deviation) for the campaign were: 28.9±3.2°C ambient temperature, 78.0±13.7% ambient relative humidity, 997±4 hPa ambient pressure, 1.8±1.2 $m s^{-1}$ local wind speed, 143±53° local wind direction.

The main aerosol inlet used in this study was equipped with a Rupprecht & Patashnick PM_{10} inlet that was optimized for isokinetic flow conditions with a cyclone (flow rate 16.7 $L min^{-1}$). The sample flow passed through stainless steel tubing (1.9 cm, 5.1 m) and a diffusion dryer with silica gel/molecular sieve cartridges (alternating regeneration with dry pressurized air, regeneration cycles 15–50 min, average RH=33±7%). After drying, the sample flow was split into separate lines. One line was for the aerosol optical instruments (0.94 cm stainless steel, ∼5 m, flow rate 6 $L min^{-1}$). Another line

ACPD
8, 6845–6901, 2008

was for the aerosol sizing instruments (particle diameter $\leq 10\,\mu m$), namely a Twin Differential Mobility Particle Sizer (TDMPS, IfT) and an Aerodynamic Particle Sizer (APS, TSI 3321). The inlet, dryer and size distribution measurements were operated by the Leibniz Institute for Tropospheric Research (IfT). The present study focuses on the optical aerosol properties; a detailed discussion of the particle size distributions will be presented elsewhere.

The NO_2 measurements were required for correction of the photoacoustic spectrometer data. The NO_x, NO_y and O_3 measurements were performed using a separate inlet and sampling line, which will be described in detail elsewhere (TECO 42CTL; operated by University of Tokyo). The CO concentration was measured using a nondispersive infrared absorption instrument (Model 48, Thermo Environmental Instruments, USA; operated by University of Tokyo). The instrument was coupled with a Nafion dryer (Perma-Pure Inc., USA) to reduce the interference from water vapor (Takegawa et al., 2006).

2.2 Optical instrumentation and extensive properties

Total aerosol particle scattering coefficients ($\sigma_{s,\lambda}$) and hemispheric backscattering coefficients ($\sigma_{bs,\lambda}$) at three different wavelengths (λ=450 nm, 550 nm, and 700 nm) were measured with an integrating nephelometer (Model 3563, TSI). The nephelometer was operated at $5\,L\,min^{-1}$ with a two minute averaging time. An auto zero, where particle-free air was sampled, was performed every two hours. The nephelometer contains two temperature sensors, one relative humidity sensor and a pressure sensor. These sensors are used to report room temperature and the conditions in the measurement chamber. The relative humidity (RH) of the sample flow into the optical instruments was 31.5±4.8%. Within this range, no systematic correlation between sample flow RH and measured optical parameters was observed, indicating that the variations of drying efficiency had no significant influence on the optical measurement results. For the campaign, the average sampling pressure and temperature as measured inside the nephelometer were 996±4 hPa and 23±1°C, respectively. The campaign average for the nephelometer lamp power was 50.6±1.1 W.

The nephelometer was calibrated with filtered air and CO_2 gas as described in the instrument's manual. The calibration was performed at the beginning, middle and end of the campaign. On average, the calibration constants were within ±2% of each other. The measurement data were corrected for truncation errors and a nonlambertian light source using the Ångström exponents that were calculated as described in Sect. 2.3.1 below (Anderson et al., 1996; Anderson and Ogren, 1998). On average, the corrected values were within 15% of the measured values for the whole campaign.

The effective limit of detection (ELOD) under the current operating condition was determined for the nephelometer signals using their respective zero signals collected during the instrument's auto zeroing time. The instrument's software automatically subtracted these zero values from the measured signals and the ELOD was three times the standard deviation of the zero signals. The campaign average ELOD values can be seen in Table 1. Any value below the ELOD was discarded. In the end, 0.1% of the nephelometer data were discarded due to ELOD reasons.

The aerosol particle absorption coefficient at 532 nm ($\sigma_{a,532}$) was determined with a photoacoustic spectrometer (PAS; Desert Research Institute), which provides highly sensitive absorption measurements without interference by scattering signals. The instrument has been described elsewhere in detail (Arnott et al., 1999). Briefly, a flow of aerosol (0.8 L min^{-1}) enters into an acoustic resonator and is illuminated by laser light (Nd:YAG, λ=532 nm, 50 mW) which is modulated at the acoustic resonator frequency (1510 Hz). The light energy absorbed by the aerosol particles is re-released as heat, producing a pressure wave that is detected by a microphone. The instrument was operated with an integration time of ~10 s and calibrated with gaseous NO_2 (~1000 ppm) (Arnott et al., 2000; Schmid et al., 2006). The data were averaged for two minutes to match the time scale of the nephelometer. The instrument noise was measured on the same time scale as the signal. The overall accuracy of the PAS calibration in this study was within 10%, thus the overall accuracy of the measured PAS absorption coefficients are also ±10% (Schnaiter, 2005). A zero measurement with filtered (Acro 50 Filters, Gelman), particle-free air was performed every 10–15 min for a period of ∼1 min. The absorption coefficient that was measured during the zeroing periods was set as 0 Mm^{-1}, thereby accounting for absorption by NO_2 (and any other potential gaseous absorbers). If, however, the ambient NO_2 concentration changed during the 10–15 min sampling period following the zeroing period, the recorded aerosol particle absorption coefficients can be influenced by the changing background signal from NO_2. Thus, the photoacoustic measurement data have been corrected for ambient NO_2 concentration as described in Schmid et al. (2006), except for the periods of 1–5 July and 27–30 July, when ambient NO_2 measurement data were not available. A plot of corrected PAS data vs. uncorrected PAS data gave a linear least squares fit equation of y=0.998x+0.0755 with R^2=0.9995, n=11,251; the relative deviation between corrected and uncorrected data was on average only 1.7%. For 97.6% of the data points this deviation was less than 10%, and for only seven out of 11 251 data points did the deviation exceed 50%. Hence, the corrections due to varying NO_2 levels were generally small and it is safe to assume that the uncorrected data for the periods of 1–5 July and 27–30 July are not affected by any substantial errors.

In order to filter out data that are impacted by noise, all high noise events (noise ≥30 Mm^{-1}, e.g., due to strong external vibrations) and their corresponding data points were excluded. The measured signal and instrument noise (N) were averaged over two minutes. The ELOD was defined as three times the average noise ($\mathrm{ELOD}_{\mathrm{PAS}}=\sum_{i=1}^{n} N_i(n\sqrt{n})^1$; n=number of points; W. P. Arnott, personal communication). Any absorption coefficient data that were smaller than the ELOD for their respective time period were discarded (3% of data). The campaign average of the ELOD for the PAS can be seen in Table 1.

ACPD
8, 6845–6901, 2008

2.3 Intensive properties

2.3.1 Ångström exponent

In analogy to aerosol optical depth or extinction, the wavelength dependence of aerosol scattering coefficients can be approximated by a power law (Ångström, 1929),

$$\sigma_{s,\lambda} = \sigma_{s,\lambda r} \left(\lambda/\lambda_r\right)^{-å_s}, \tag{1}$$

where $\sigma_{s,\lambda r}$ is the scattering coefficient at a given reference wavelength λ_r, and $å_s$ is the dimensionless Ångström exponent. The Ångström exponent corresponds to the slope of a double-logarithmic plot of σ_s vs. λ as seen in Fig. 2 and is calculated according to Eq. (2).

$$å_s(\lambda_1/\lambda_2) = -\frac{\log(\sigma_{s,\lambda_1}/\sigma_{s,\lambda_2})}{\log(\lambda_1/\lambda_2)} \tag{2}$$

If this plot is linear, as shown in Fig. 2a, then $å_s$ is independent of λ. However, $å_s$ can exhibit a dependency on λ, as seen in Fig. 2b. This wavelength dependence is characterized by the curvature seen in Fig. 2b and quantified by the second derivative of the double-logarithmic plot of σ_s vs. λ (i.e., the first derivative of the Ångström exponent) as $å'_s$. The second derivative for the wavelength interval centered around 550 nm, $å'_s$ (550), has been approximated by Eq. (3) (Li et al., 1993; Eck et al., 1999).

$$å'_s(550) = \left(\frac{2}{\log(450/700)}\right)\left(å_s(450/550) - å_s(550/700)\right) \tag{3}$$

In this study, the measured scattering coefficients have been used to calculate Ångström exponent values ($å_s(\lambda_1/\lambda_2)$) for the wavelength pairs of 450/550 nm, 550/700 nm, and 450/700 nm. The curvature was quantified using these $å_s$ values to calculate the $å'_s$.

ACPD

8, 6845–6901, 2008

The second derivative values (å′) reported in the literature generally use the Ångström exponent calculated from extinction coefficients (å$_e$), while in the current study, the scattering coefficients were used as indicated by the "s" subscript. When comparing å$'_s$ and å$'_e$, it is possible that differences might arise from a potential wavelength dependence of absorption. This was investigated by converting σ_s into extinction coefficients ($\sigma_e = \sigma_s + \sigma_a$) at all three wavelengths (450 nm, 550 nm and 700 nm) using $\sigma_{a,532}$ and assuming a λ^{-1} and λ^{-2} wavelength dependence of absorption. The å$_e$ and å$'_e$ values were then calculated in analogy to Eqs. (2) and (3).

2.3.2 Backscattering fraction and single scattering albedo

The angular corrected backscattering coefficient from the nephelometer is the scattered light intensity in the backward hemisphere of the particle (90–180°) (Anderson and Ogren, 1998). The hemispheric backscattering fraction, b_λ, is the ratio of this backscattering coefficient over total scattering coefficient at a given wavelengths (λ=450, 550, and 700 nm).

$$b_\lambda = \frac{\sigma_{bs,\lambda}}{\sigma_{s,\lambda}} \tag{4}$$

The single scattering albedo, ω_λ, is the ratio of the scattering coefficient over the extinction coefficient at a given wavelength. Here ω has been calculated at λ=532 nm using Eq. (5).

$$\omega_{532} = \frac{\sigma_{s,532}}{\sigma_{s,532} + \sigma_{a,532}} \tag{5}$$

The $\sigma_{s,532}$ was not measured directly by the nephelometer, but rather was calculated using Eq. (2) with the inputs, å$_s$=å$_s$ (550/700) $\sigma_{s,\lambda 1} = \sigma_{s,550}$ and with λ_1=550 nm and λ_2=532 nm. Test calculations using å$_s$ (450/700) and å$_s$ (450/550) instead of å$_s$ (550/700) gave only slightly different results (relative deviations in $\sigma_{s,532}$<1%).

3 Results and discussion

3.1 Overview of optical measurement results (time series & statistical distribution)

Figure 3 shows the time series of the aerosol particle total scattering, backscattering and absorption coefficients for the green spectral range ($\sigma_{s,550}$, $\sigma_{bs,550}$, $\sigma_{a,532}$) throughout the measurement campaign. The scattering and backscattering coefficients at λ=450 nm and 700 nm ($\sigma_{s,450}$, $\sigma_{bs,450}$, $\sigma_{s,700}$, $\sigma_{bs,700}$) followed essentially the same trends as those for 550 nm.

All extensive optical parameters exhibited very high variability ranging from the instrument detection limits on rainy days such as 17 July to extremely high values during a heavy pollution episode on 23–25 July characterized by intense local biomass burning of farming plant waste. In order to accurately describe the average optical properties of this measurement site, the data from the time period of 23–25 July 2006 were excluded from the calculation of campaign averages and all data analyses in this paper, unless stated otherwise. During this period, the source of the pollution was evident (local farmers burning their plant waste), unique (never again during the campaign did such intense burning occur) and the period was well defined (it began shortly after a power outage on 22 July and ended with an intense rain event ~21:15 on 25 July).

The differences between the campaign averages with and without 23–25 July 2006 are shown in Table 1. For example, the relative standard deviation of $\sigma_{s,550}$ is 68% without the 23–25 July data and 104% with all the data included. Thus some of the large variation in the extensive parameters can be attributed to this highly polluted period. However, even with this period excluded, the variation in the data remains high.

Figure 4 summarizes the statistical distribution of the nephelometer data for the whole campaign, excluding 23–25 July. The mean and median values are represented by the dot and line in the box, respectively, and the top and bottom of the box are the 75th and 25th percentiles, respectively. The error bars indicate the 95th and 5th percentile. All similar statistical box plots shown in this paper will have the same structure.

The mean values of the σ_s and σ_{bs} coefficients are generally well above the median

ACPD
8, 6845–6901, 2008

value. For example, the median value for $\sigma_{s,550}$ is 123 Mm^{-1} while the mean value is 151 Mm^{-1}, which is 23% larger than the median value. This difference indicates a non-Gaussian distribution of the data with some very large values (i.e., during pollution episodes).

The Ångström exponent ($å_s$), backscattering fraction (b), and single scattering albedo (ω_{532}) time series are shown in Fig. 5. These parameters were calculated as described in Sect. 2.3. The major polluted period of the campaign, 23–25 July, can be seen clearly in the backscattering fraction and Ångström exponent time series with a sudden decrease at the beginning of this time period and continued low values throughout the episode. This highlights the fact that the particles measured during this time had different optical properties from the rest of the campaign; again these data were removed from the discussion of the average optical properties.

Figure 6 displays box plots for the campaign statistics of b, $å_s$ and $\sigma_{s,532}$, $\sigma_{a,532}$ and ω_{532}. The mean values and standard deviations of b were 0.116±0.013 (450 nm), 0.124±0.015 (550 nm), and 0.154±0.017 (700 nm); and for $å_s$ were 1.51±0.22 ($å_s$ (550/700)), 1.46±0.21 ($å_s$ (450/700)) and 1.38±0.22 ($å_s$ (450/550)). As seen in Fig. 6a and b, both b and $å_s$ were dependent on wavelength. While b increased with increasing wavelength due to decreasing size parameters, $å_s$ increased for the longer wavelength pairs due to curvature in the log (σ_{sp}/Mm^{-1}) vs. log (λ/nm) plot. The latter will be discussed in detail in Sect. 3.3.2.

In Figure 6c, the calculated $\sigma_{s,532}$ and measured $\sigma_{a,532}$ values are displayed. These two coefficients were used to calculate ω_{532}, which is also shown in Fig. 6c. The mean and standard deviation of $\sigma_{s,532}$ for the campaign was 158±108 Mm^{-1}, slightly larger than the measured $\sigma_{s,550}$. The mean and standard deviation for ω_{532} for the campaign was 0.82±0.07. Note that for the intensive parameters b, $å_s$ and ω_{532} the relative standard deviations are small (≤16%) compared to the extensive parameters (σ_s and σ_a) and the distribution is symmetric, i.e., the mean and median values are similar (within 2%). This suggests that most of the observed variation in the extensive optical properties was due to changes in the particle concentration rather than in changes in the intrinsic optical properties of the particles.

During the highly polluted period of 23–25 July 2006 ("smoky period"), the extensive properties were up to four times larger than during the rest of the campaign (average relative increase: +300% for σ_s, +250% for σ_{bs}, +200% for σ_a). The Ångström exponent for two of the wavelength pairs increased during the smoky period (+8% for 550/700 nm, +3% for 450/700 nm), but decreased for the third pair (–4% for 450/550 nm). These differences in percent difference can be explained by increased curvature and will be discussed in Sect. 3.3.2. The single scattering albedo increased during this time to 0.88, which is common in smoldering fires (Reid, 1998). The parameters determined during the smoky period can be considered to represent the optical properties of emissions from the burning of plant farming waste.

Table 2 summarizes the scattering and absorption coefficients and single scattering albedos observed in this study and in select other studies using similar instrumentation (Quinn et al., 1998; Anderson et al., 1999; Bergin et al., 2001; Andreae et al., 2002; Xu et al., 2002; Anderson et al., 2003; Adam et al., 2004; Kim et al., 2004; Quinn et al., 2004; Malm et al., 2005; Cheng et al., 2006; Fujitani et al., 2007; Li et al., 2007; Wang et al., 2007; Andreae et al., 2008). The measured $\sigma_{s,550}$ values at the Backgarden site (this campaign) are lower than most measurements made in urban areas in Asia; however, they are still larger than results from many other urban areas (e.g., Baltimore and Atlanta). The average σ_a from this study is also smaller than the σ_a measured in large urban areas in Asia, though similar to urban areas elsewhere. Since the concentrations of black carbon (BC) in Southern China are normally at their lowest in summer (Streets et al., 2003; Cheng et al., 2006), the average absorption values measured in this campaign may represent the annual low for this area. Compared to the other campaigns listed in Table 2 the ω values measured in Backgarden are among the lowest, indicating darker (i.e., more highly absorbing) aerosols and a higher relative abundance of LAC and combustion sources in the PRD.

The ω values reported in Table 2 are for a variety of relative humidities; many of which are for dry aerosols. In order to convert to atmospheric relevant conditions, the hygroscopic growth of these aerosol particles and its impact on their light scattering and absorption would need to be quantified, which is beyond the scope of this manuscript.

3.2 Diurnal variations

The σ_s, σ_a ω_{532} and $å_s$ values were found to have pronounced diurnal variations. Figure 7a and b display the statistics for the normalized $\sigma_{s,550}$ and $\sigma_{a,532}$. To normalize the data, each measured value was divided by its respective 24-h average (arithmetic mean) on the day of measurement. Thus, in Fig. 7a and b, a value of one indicates the daily average. The $\sigma_{s,550}$ was elevated during the nighttime with a maximum mean value of 1.2 (20:00–22:00). Both the mean and median values then fall below one between 8:00 and 18:00 with a minimum mean value of ~0.8 between 9:00 and 14:00. Figure 7b displays the diurnal cycle for $\sigma_{a,532}$, which is even more pronounced than that of $\sigma_{s,550}$. Again, both the mean and median values were enhanced at night with maximum hourly mean values of 1.3 (19:00–21:00) and 1.4 (6:00). The mean and median values then fall below one between 8:00 and 18:00 with a minimum hourly mean value of ~0.6 between 10:00 and 15:00.

For comparison, Fig. 7c and d display the diurnal cycles of the gas phase concentrations of NO_y and CO, respectively. Both exhibited similar cycles with minima during the day and maxima at night with a build-up evident before sunrise and a sharp decrease around sunrise (6:00–8:00). Similar to the $\sigma_{a,532}$ cycle, the daytime minimum concentration of CO was on average ~40% lower than the corresponding 24-h mean value. The NO_y daytime minimum concentration was on average ~50% lower than the 24-h mean.

Most likely, the diurnal cycles of $\sigma_{s,550}$, $\sigma_{a,532}$, NO_y, and CO were dominated by convective mixing during the daytime, which leads to a dilution and decrease in $\sigma_{s,550}$, $\sigma_{a,532}$ and trace gas concentrations. After sunset, the formation of a stable nocturnal boundary layer (BL) in combination with the continued emission or advection of particles and trace gases throughout the night, leads to an increase in $\sigma_{s,550}$, $\sigma_{a,532}$ and gas phase concentrations. As this measurement campaign was in the summer, it is unlikely that the increase observed in the evening was caused by an increase of local or regional emissions from biomass burning or heating fuel combustion. While there were no local rush hours with enhanced traffic emissions, it is evident from Fig. 1 that the site is only some 10 km downwind of densely populated and industrialized areas of the Guangzhou urban area. Since truck traffic, dominated by high-emission diesel vehicles, increases sharply at night as a result of local traffic regulations (Bradsher, 2007), increased diesel emissions in the upwind area must be expected and probably contribute to the evening increase in pollutants at our site. Thus, the diurnal cycle of the extensive optical properties appears to be driven by the changes in the boundary layer in combination with enhanced diesel emissions at night.

As seen in Fig. 8a, the diurnal cycle observed for ω_{532} is a mirror image of the $\sigma_{a,532}$ cycle. The maximum hourly mean values (0.86–0.87) occurred during the daytime (10:00–14:00) and the minimum hourly mean values (0.79–0.80) occurred in the morning (5:00–6:00) and evening (19:00–20:00). Additionally, around sunrise (6:00–8:00) the ω_{532} values sharply increased, just as the $\sigma_{a,532}$ and $\sigma_{s,550}$ values sharply decreased, reached a plateau at 10:00 and stayed constant until 16:00. If a combination of convective mixing and regional emissions is responsible for the diurnal cycle of ω_{532}, it can be described by a simple conceptual mixing model (Fig. 9) (Keeling et al., 1996). One end-member of the mixing series would be the daytime aerosol particles present in the well-mixed BL at the middle of the day, the other an aerosol representing fresh emissions with a lower ω_{532}. In a plot of $\sigma_{a,532}$ vs. $\sigma_{s,532}$, the hourly mean values would move from a daytime value, reflecting the BL average ω_{532}, along a line with a slope defined by the ω_{532} of the fresh emissions, towards a set of points that represent the composition of the aerosol in the nocturnal BL (Fig. 9). The residual layer above the inversion would continue to contain the more highly aged daytime particles with a higher ω_{532}. When convective mixing begins after sunrise, these two types of aerosols would mix, and the ω_{532} values measured through the morning would be a linear combination of the "night" aerosol particles with a low ω_{532} and the "day" aerosol particles with a high ω_{532}. Any significant deviation from a straight mixing line would indicate addition (or removal) of an aerosol component with a different ω_{532} (e.g., by secondary aerosol formation).

To test this assumption, the hourly mean $\sigma_{a,532}$ and $\sigma_{s,532}$ values were plotted in Fig. 9 (points are labeled as "time of day"). The average value of the 06:00 and 07:00 means (point N in Fig. 9) was assumed to represent the nighttime conditions before the onset of convective mixing, and the mean value at 12:00 (point D) was taken to be representative of the fully mixed daytime BL. Lines were fit through each of these points and forced through the origin. The slope of these lines, $a=d\sigma_{a,532}/d\sigma_{s,532}$, is related to ω_{532} by $\omega_{532}=1/(a+1)$, and thus reflects the characteristic ω_{532} of the day and night aerosol. Figure 9 shows that all of the values during nighttime are clustered towards the top right around the 20:00 value. After sunrise, the values move down the mixing line to the 12:00 value, consistent with the assumption that convective mixing can explain the morning drop in $\sigma_{a,532}$ and $\sigma_{s,532}$, as well as the concurrent drop in ω_{532}.

The return path from D to N suggests a slight curvature, which may be related to local production of secondary aerosol mass in the early afternoon hours. However, the variability in the data does not permit a firm conclusion regarding the significance and amount of secondary aerosol production. At any rate, our results show no clear evidence of strong in-situ production of secondary aerosol mass on a time scale of hours, and, within the experimental uncertainty, the observed behavior can be adequately explained by mixing of fresh emissions and aged aerosol. If we assume the data in Fig. 9 to represent only the mixing between one end-member representing a mixed regional BL aerosol and another representing fresh pollution, the single scattering albedo of this second component can be derived from the slope of the mixing line. Linear regression to the data yields a slope of 0.44 corresponding to $\omega_{532}=0.69$.

The diurnal cycle for $å_s$ (450/700) is displayed in Fig. 8b. The mean values have a minimum of 1.33 in the morning (5:00–7:00) and a maximum value of 1.65 in the afternoon (15:00–16:00). It indicates that the aerosol particles were on average smaller in the afternoon, which might be due to new particle formation or temperature-related gas-particle partitioning effects.

For comparison, Fig. 8c and d display the diurnal cycles of ozone and ambient temperature, respectively. Additionally, Fig. 8c displays the rate of change in $[O_3]$ as a function of time, which can be considered an indication of photochemical activity. This rate was calculated by fitting a Gaussian curve to the mean hourly $[O_3]$ (shown in Fig. 8c) and taking the derivative of the fit. This is reported in ppb min^{-1} by the dotted line on Fig. 8c and indicates that the photochemical activity (represented here by $d[O_3]/dt$) is highest before noon, while the concentration of ozone is highest in the early afternoon. Note that this peak in ozone concentration corresponds to both the increased scattering seen in the afternoon in Fig. 9 as well as the peak in the $å_s$ cycle. If secondary aerosol production is responsible for the afternoon increase of scattering and decrease of average particle size, then this production is not occurring at the peak of photochemical activity, but rather at the peak of $[O_3]$. Additionally, the $å_s$ cycle is similar to the temperature diurnal cycle. It is possible that the temperature increase might lead to a reduction of particle size by evaporation of semi-volatile components. However, further investigations into the diurnal cycle of the aerosol size distributions and composition as well as detailed modeling of the gas phase and heterogeneous chemistry will be required to fully elucidate the diurnal cycle of $å_s$.

During the campaign there was a tropical storm, Bilis (15 to 17 July), a typhoon, Kaemi (25 July 21:00 to 27 July) and one large rain event (10 July 13:15 to 11 July 19:00). These periods may change the aerosol properties and thus may influence the apparent diurnal patterns. When excluding these periods, the mean and median values of the ω_{532} and $å_s$ changed by less than 2%, and the diurnal cycles did not change at all. For the purpose of radiative calculations in climate models, the ω_{532} of average dry aerosol particles in the PRD region appears best represented by the daytime average value of 0.87 (also represented by the line from the origin through point D in Fig. 9), which is somewhat higher than the 24-h average of 0.82 (Table 2). The daytime measurements most closely reflect the mean composition of the boundary layer and represent the aerosol that actually interacts with the solar radiation.

ACPD

8, 6845–6901, 2008

Title Page
Abstract Introduction
Conclusions References
Tables Figures
◀ ▶
Back Close
Full Screen / Esc
Printer-friendly Version
Interactive Discussion

Correlations with wind direction and air mass trajectories

The local wind direction and wind speed (υ) were measured by a Vaisala Weather Transmitter (WXT510; operated by University of Tokyo). Figure 10 shows the correlation of $\sigma_{s,550}$ and ω_{532} to local wind direction and local wind speed. On these graphs, Guangzhou would be ~157°. Figure 10a is wind direction versus wind speed, with $\sigma_{s,550}$ as the color scale. No strong correlation was seen between $\sigma_{s,550}$ (and $\sigma_{a,532}$, though not shown) and local wind direction. On average, both $\sigma_{s,550}$ and $\sigma_{a,532}$ were lower during periods with above average local wind speeds (wind speed (υ)≥2 m s^{-1}). When υ<2 m s^{-1}, the average $\sigma_{s,550}$ was 128 Mm^{-1} compared to 82 Mm^{-1} when υ≥2 m s^{-1}. Similarly, $\sigma_{a,532}$ was higher when υ<2 m s^{-1} with an average value of 42 Mm^{-1} compared to 21 Mm^{-1} when υ≥2 m s^{-1}. Many of these instances of high wind speed were during storms when rain was also present.

Figure 10b displays wind direction versus ω_{532}. Average ω_{532} values (0.8–0.9) are not correlated with wind direction. However, the lower values (0.6–0.8) were seen mostly when the wind was coming from 45–180°. When the local wind was coming from this direction, almost half (44%) of the ω_{532} values recorded were in the range of 0.6–0.8. This is compared to only 16% of the recorded ω_{532} values in the range of 0.6–0.8 when the local wind was from the 180–45° direction. This correlation with ω_{532} suggests that there may be a source of absorbing aerosols in this south/easterly (45–180°) direction, coinciding with the location of the densely populated urban region and high heavy-duty vehicle traffic (Fig. 1). Besides these weak relationships, no parameter was clearly correlated with local wind direction, indicating that the aerosol sources and pollution are regional in nature.

In order to probe the relationship of air mass origin and optical properties, nine days were chosen to represent the variety of wind trajectories that occurred throughout the campaign. Back trajectories were calculated with the NOAA Hysplit model (Draxler and Rolph, 2003) using FNL meteorological data (Stunder, 1997). Figure 11a displays the 24-h back trajectories (start: 24:00 local time, elevation: 100 m) for these nine

ACPD
8, 6845–6901, 2008

Title Page
Abstract Introduction
Conclusions References
Tables Figures
◀◀ ▶▶
◀ ▶
Back Close
Full Screen / Esc
Printer-friendly Version
Interactive Discussion

days. With the exception of 13 and 28 July, the calculated back trajectories were similar throughout the day (start times: 00:00–24:00). Back trajectories calculated every four hours for 13 and 28 July are shown in Fig. 11b. For 13 July, the trajectory indicates that the air masses came from the west in the morning (red-light green) with a counterclockwise motion, and then moved to the north as the day continues. On 28 July, the air masses in the morning came from the coast, but moved farther out to sea as the day went on. Additionally, the trajectories on 12 July varied slightly (not shown). All trajectories on this day showed the air masses originating from the south of the measurement site; however the counterclockwise movement, as seen in Fig. 11a for this day, started at 15:00 local time. Before that time, the trajectories were calculated to come in directly from the south. Overall, 83% of the back trajectories calculated for the campaign originated from the south (90–180°).

Table 3 displays the daily averages of both extensive and intensive properties for these highlighted days. 12 July had the highest daily average for both σ_s and σ_a. On this day there was a strong counterclockwise movement of the calculated trajectories, influenced by the incoming typhoon Bilis, indicating that these air masses moved slowly and more than once over the same local, continental sources. This combination of slow winds, repetitive crossings over pollution sources and 24 h over land led to a polluted air mass with the highest 24-h average σ_s and σ_a.

In the morning of 13 July we observed the highest 2-minute average scattering and absorption coefficients and the lowest single scattering albedo of the campaign (excluding 23–25 July): $\sigma_{s,550}$=1132 Mm^{-1}, $\sigma_{a,532}$=305 Mm^{-1}, ω_{532}=0.48. Note that this scattering coefficient is similar to the values reported from dust storms (e.g., $\sigma_{s,530}$=1139 Mm^{-1} measured in Korea in the outflow of a dust storm in China (Kim, He et al., 2004)).

13 July was one of only five days that had back trajectories originating from the north and were thus strongly influenced by continental sources. Additionally, as seen in Fig. 11b, there was also strong counterclockwise motion early in the day when the values were the highest (the red and green trajectories), indicating that, similar to 12

July, these air masses moved slowly over the same local sources.

Both 20 and 21 July were characterized by low wind speeds and back trajectories from the S/SW. 10 July has trajectories from S/SE and there were also heavy rains in the afternoon, starting 13:15 and continuing until the next day. 3, 4, 18 and 28 July were unique in that their back trajectories both showed a higher wind speed and came directly off of the sea from the south and southeast. Also, 3, 4 and 18 July were calculated to pass over the Guangzhou/PRD region.

As seen in Table 3, when the air mass was over land for more than 24 h (i.e., 12, 13, 20 and 21 July), the extensive properties were the highest, indicating higher aerosol concentrations. When the air mass spent less than 24 h over land (3, 4, 18 and 28 July) the extensive optical properties were lower and were below the campaign averages (Table 1). During the same periods, the ω_{532} values also were lower than when the air mass spent more time over land. These low values of ω_{532} and the low extensive properties are consistent with measuring mainly primary emissions that are higher in absorbing material (e.g., soot), yet show lower extensive properties due to a short residence time over the source region (PRD). In contrast, the highest ω_{532} values were measured on 12 and 20 July when the air masses were slowly moving and hence residing longer over local continental sources, which resulted in elevated aerosol concentration (high extensive properties) and photochemical aging (high single scattering albedo). In contrast to the extensive properties and ω, the $å_s$ and b_{550} values did not show a strong dependence on either the direction or the time spent over land of the calculated back trajectories.

3.3 Correlation with size distribution and CO

3.3.1 Mass scattering and absorption efficiency

The size distribution of PM_{10} aerosol was measured from the same inlet as the aerosol optical measurements. From the integrated size distribution and assuming a density of 1.7 g cm^{-3}, the PM_{10} mass was calculated. Figure 12 displays the scattering and absorption coefficients plotted versus PM_{10} mass concentrations measured during the campaign (excluding 23–25 July). The slopes of the fit lines can be regarded as the PM_{10} mass scattering efficiency α_s=2.84±0.037 m^2 g^{-1} and mass absorption efficiency α_a=0.74±0.009 m^2 g^{-1}, respectively (reduced major axis best fit; Ayers, 2001; Hammer et al., 2001). The scattering and absorption efficiencies derived from the fit lines are higher than the arithmetic mean values but within the standard deviations calculated from the individual data points (α_s=2.41±0.79 m^2 g^{-1}, α_a=0.52±0.22 m^2 g^{-1}).

The observed α_s values are in the range of literature data characteristic for urban areas. The IPCC report (2001) recommends a value of 1.0–3.5 m^2 g^{-1} for urban areas, depending on pollution levels and particle size distribution. Waggoner et al. (1981) found a similar range of 2.23–2.94 m^2 g^{-1} (PM_3) for a variety of cities in the United States. Bergin et al. (2001) reported a value 2.3–3.6 m^2 g^{-1} (PM_{10}) for Beijing aerosol. Adam et al. (2004) reported values of 0.365–2.05 m^2 g^{-1} (total suspended particles, ambient RH) for urban Baltimore.

3.3.2 Ångström curvature

The Ångström exponent ($å_s$) is a parameter that is easily obtained through a variety of techniques, i.e., sun photometry, nephelometry and satellite retrievals (e.g., Nakajima and Higurashi, 1998; Eck et al., 1999; Carrico et al., 2003; Quinn and Bates, 2005) As such, it is useful to use $å_s$ to elucidate other, more difficult to measure, parameters. Many studies have used the wavelength dependence of $å_s$ to gain information on the size distribution of the particles (e.g., Eck et al., 1999; 2001; Schuster et al., 2006; Gobbi et al., 2007). Many of these studies did not have direct measurements of the aerosol size distribution, but rather used retrievals from sun photometers (Eck et al., 1999; 2001). In this measurement campaign, optical and size distribution measurements were obtained from the same inlet. To our knowledge, this is the first study to quantify the Ångström curvature with simultaneous nephelometer and size distribution measurements.

Figure 2 displays the log (σ_s/Mm^{-1}) vs. log (λ/nm) plots for 18 July, a relatively clean day, and 25 July 2006, during the local biomass burning event (smoky period). The dotted line is a linear fit and the solid line is the second-order polynomial from King and Byrne (1976). The slope of the linear fit is used to calculate $å_s$ using Eq. (2). As seen in Fig. 2, the linear relationship fits the data adequately (Fig. 2a) when there is no curvature. In Fig. 2b the second-order polynomial can properly capture the curvature in the log (σ_s/Mm^{-1}) vs. log (λ/nm) plot. This curvature leads to different calculated $å_s$ from Eq. (2) for different wavelength pairs. For example, the daily averages for 25 July were 1.36±0.07 ($å_s$ (550/700)), 1.21±0.07 ($å_s$ (450/700)) and 1.03±0.07 ($å_s$ (450/550)). Figure 13 displays the time series of $å_s$ for two different wavelength pairs, $å_s$ (550/700) and $å_s$ (450/550). While these values are very similar for some periods, they are different for others. The difference between these $å_s$ values is expressed by the first derivative of $å_s$ ($å_s'(\lambda_{550})$), which is the second derivative of log (σ_s/Mm^{-1}) vs. log (λ/nm) calculated according to Eq. (3) (Li et al., 1993; Eck et al., 1999); throughout this discussion $å_s'(\lambda_{550})$ will be referred to as the "second derivative".

The second derivative describes the curvature in the log (σ_s/Mm^{-1}) vs. log (λ/nm) plot. For example, Fig. 2 illustrates a positive curvature in the 25 July data corresponding to $å_s'$=3.44±0.26. The campaign average of $å_s'$ is 1.54±1.40, indicating that, on average there is less curvature than during the highly polluted days. Almost no curvature was seen on 18 July ($å_s'$=−0.040±0.71). To our knowledge, the second derivative observed on 25 July is the highest reported for atmospheric aerosols. It is substantially larger than the second derivative values reported for biomass burning aerosol in Bolivia ($å_e'$ 2.09; Eck et al., 1999) and in Zambia ($å_e'$<2.2; Eck et al., 2001). The campaign average is similar to values Eck et al. (1999) measured in an urban site in the eastern US (1.10 and 1.76).

The time series of $\sigma_{s,550}$ was also included in Fig. 13 to highlight the polluted periods. As seen from Fig. 13, the second derivative has non-zero values around the more polluted periods (i.e., 12–13 July 2006 and 23–25 July 2006), though the second derivative is non-zero for longer periods than just during the pollution. This suggests that the driving force for the curvature is not only the pollution level. Figure 14 displays the dependence of the second derivative on pollution level, represented here by total scattering. At lower scattering values (<500 Mm^{-1}), the second derivative tends to increase dramatically with increasing scattering, while almost constant values for the second derivative of ~3 occurred for $\sigma_{s,550}$>500 Mm^{-1}.

Using other ground based techniques (i.e., sun photometers) it has been suggested that the main driving force of the curvature is the fine/coarse ratio of the size distribution (e.g., Eck et al., 1999; Schuster et al., 2006; Gobbi et al., 2007). Figure 15 displays the second derivative as a function of the submicron aerosol fraction (fine D_p<1 μm). All of the campaign data is included in this graph, including 23–25 July. The data are color coded for the day of measurement. Generally, there is an increase in the second derivative with an increase in fine fraction. Additionally, all of the data except 10 July (the green points to the left of the majority of the data) have a very similar relationship between the second derivative and fine fraction; for these days, the curvature in $å_s$ can be explained by an increase in the fine fraction. On 10 July there was a greater increase in the PM_{10} mass than in the PM_1 mass and thus the PM_1/PM_{10} fraction is the lowest in this campaign. It is currently not clear what caused this exceptional increase in PM_{10} mass; a measurement artifact cannot be excluded, but we have no other evidence for it.

Differences between Ångström exponents and curvatures derived from scattering and extinction measurements have been tested as described in Sect. 2.3.1. For 25 July, 18 July and for the entire campaign, the average second derivative values referring to extinction are 2.56±0.37, −0.044±0.54 and 1.06±1.07, respectively, when absorption is assumed to be proportional to λ^{-1}. Assuming a λ^{-2} dependence of absorption yields only slightly different values (2.50±0.39, −0.12±0.63 and 1.07±1.10, respectively).

The second derivative values referring to extinction are about 30% lower than those referring to the scattering coefficient. However, there is still a curvature for 25 July and the campaign average as the second derivative is still greater than zero. Thus, for PRD aerosol, absorption introduces only a small difference between the curvatures of the extinction and scattering coefficients as a function of wavelength. Only in regions where the single scattering albedo is considerably lower could absorption introduce a large difference in curvatures.

3.3.3 Correlation of absorption coefficient and CO concentration

The absorption coefficient (σ_a) is a measure of the amount of light absorbing material in the aerosol. In general, this material is composed of carbon containing compounds that are referred to as light absorbing carbon (LAC) (Andreae and Gelencser, 2006), but mineral components, such as those contained in desert dust, may also contribute to aerosol absorption (Jennings et al., 1996; Fialho et al., 2005). In the following discussion it will be assumed that the absorption coefficient was dictated by the LAC concentration with a single mass absorption efficiency value of 7.5 $m^2\,g^{-1}$, which refers to uncoated, fully graphitized soot (Bond, 2006). Therefore the calculated LAC concentration should be considered as an upper limit estimate.

A major source of LAC is combustion of fossil fuels and biomass, during which both LAC and CO are released. Consequently, strong correlations between LAC mass and [CO] have been seen in other urban areas (Chen et al., 2001; Baumgardner, 2002; Lim, 2002; Park, 2005; Kondo et al., 2006; Baumgardner, 2007), although in these studies instrumentation other than the PAS were used, and thus the Elemental Carbon (EC) mass was reported. Since the ratio of LAC mass to [CO] is highly dependent upon many factors including the type and proximity of combustion source, combustion conditions and the presence of dust, these previous studies have found the ratio to differ significantly between cities and seasons (Chen et al., 2001; Baumgardner, 2002; Lim, 2002; Park, 2005; Kondo et al., 2006; Baumgardner, 2007).

Figure 16 displays the correlation between LAC mass and [CO] obtained for this study. The ΔLAC/ΔCO values were calculated as described in Kondo et al. (2006). The background LAC and CO levels, LAC_0 and CO_0, were assumed to be the 1.25th percentile value and the ΔLAC/ΔCO values were calculated in three ways; (1) the slope of LAC mass vs. [CO] reduced major axis linear fit (Fig. 16); (2) the slope of a linear fit, forced through zero, of LAC-LAC$_0$ vs. CO-CO$_0$; (3) the median value of (LAC-LAC$_0$)/(CO-CO$_0$) with all values where CO-CO$_0$<100 ppb excluded. The three methods produced ΔLAC/ΔCO values of 6.94±0.07 ng m^{-3} ppb^{-1}, 4.96±0.05 ng m^{-3} ppb^{-1} and 6.45±9.21 ng m^{-3} ppb^{-1}, respectively. These values are similar to values measured in Guangzhou during the PRIDE-PRD2004 campaign (7.9±0.5 ng m^{-3} ppb^{1}) (Andreae et al., 2008) as well as in the Japanese cities of Nagoya (6.3±0.5 ng m^{-3} ppb^{-1}) and Tokyo (5.7±0.9 ng m^{-3} ppb^{-1}) (Kondo et al., 2006). Much smaller values were measured in Mexico City (1.63–2.23 ng m^{-3} ppb^{-1}) (Baumgardner, 2002; Jiang et al., 2005; Baumgardner, 2007), Baltimore (2.3±0.8 ng m^{-3} ppb^{-1}) (Park, 2005) and Atlanta (3.2 ng m^{-3} ppb^{-1}) (Lim, 2002). Additionally, smaller values were also measured in the fall, winter and spring months in Fort Meade, Maryland 2.7 ng m^{-3} ppb^{-1}, 2.9 ng m^{-3} ppb^{-1} and 2.7 ng m^{-3} ppb^{-1}, respectively, though similar values to this study were measured there in the summer (4.1–6.7 ng m^{-3} ppb^{-1}) (Chen et al., 2001).

Figure 16 displays the uncorrected LAC mass vs. [CO] data with the reduced major axis fit and boundary conditions. The slope of the lines shown on Fig. 16 (ΔLAC/ΔCO) range from 0.498 to 48.5 ng m^{-3} ppb^{-1}. No study, to our knowledge, has reported as high values as our upper boundary, 48.5 ng m^{-3} ppb^{-1} and even the averages reported above are among the higher values measured. In order to determine whether unique conditions were causing these high values, the time and day when ΔLAC/ΔCO was greater than 8 ng m^{-3} ppb^{-1} were probed. 65% of the values over 8 ng m^{-3} ppb^{-1} occurred during the nighttime (18:00–7:00), with 77% of these high nighttime values occurring either in the early morning (4:00–6:59) or evening (19:00–21:59), close to the times of highest truck traffic in the region. These values were present on every day where both CO and LAC were measured, thus these high ΔLAC/ΔCO events are not unusual for this area, but a daily occurrence. These values could be produced through relatively efficient combustion with low CO concentrations and high emissions of LAC. Additionally, the high ΔLAC/ΔCO values could be due to absorption enhancement (higher LAC absorption efficiency) as was observed for coated versus uncoated soot particles (Saathoff et al., 2003) or to non-combustion sources of light absorbing particulate matter. The large range of ΔLAC/ΔCO values measured during this campaign suggests a variety of sources for both absorbing aerosols and CO in the PRD region.

3.4 Radiative forcing sensitivities

By scattering and absorbing incoming solar radiation, aerosols can impact the radiative balance and cool the surface of the Earth. The cooling potential of aerosol particles generally increases with increasing single scattering albedo and backscattering fraction.

Figure 17 displays ϖ_{532} versus b_{550} for this campaign (including 23–25 July) with the color scale as local time. There are three lines on the graph to describe an upper and lower boundary as well as a fit through the bulk of the data. The black line (y=−3.58x+1.27) is a fit forced through the data point with the highest ϖ_{532} and lowest b_{550} to capture the bulk of the data as well as the data with high ϖ_{532}. The blue (y=−0.754x+1.03) and red (y=−12.07x+1.98) lines are not fits through the data, but rather represent the approximate boundaries of the data. The data that are clustered at the top left hand side of the graph, where the lines meet, were all measured during the day on 25 July (~10:00–17:00) which is during the biomass burning event. Additionally, as can be seen by the color coding in Fig. 17, the colors are not distributed evenly, but rather each time period has its own relationship between ϖ_{532} and b_{550}. For this reason we have chosen the two boundary conditions and the middle fit to test the sensitivity of radiative forcing on various ϖ_{532} vs. b_{550} trends; hence, the lines are not meant to describe the whole data set, but rather describe the range of realistic ϖ_{532} vs. b_{550} conditions.

Since ϖ_{532} and b_{550} are negatively correlated (Fig. 17), they partially offset their respective radiative forcing as an increasing b_{550} indicates increased cooling while a decreasing ϖ_{532} indicates increased warming. This negative correlation has been previously noted in Reid and Hobbs (1998), however the impact of this relationship on radiative forcing was not discussed.

The radiative forcing equation from Haywood and Shine (1995) was used to investigate how this coupling will impact the aerosol particles' forcing (Eq. 6).

$$\Delta F/\delta \approx -DS_o T_{\text{atm}}^2 (1 - A_c)\omega\beta\{(1 - R_s)^2 - (2R_s/\beta)\left[(1/\omega) - 1\right]\} \quad (6)$$

The aerosol radiative forcing efficiency ($\Delta F/\delta$) is defined as the forcing per unit aerosol optical depth. In order to use Eq. (6) to test the sensitivity of the coupling of ω_{532} and b_{550}, the other terms in the equation were assumed to be constant and have the following values: fractional daylight D=0.5, solar flux S_o=1370 W m^{-2}, atmospheric transmission T_{atm}=0.76, fractional cloud amount A_c=0.6, surface reflectance R_s=0.15. The upscatter fraction β was calculated from b_{550} using the parameterization of Wiscombe and Grams (1976) in Sheridan and Ogren (1999).

Figure 18a displays $\Delta F/\delta$ as a function of b_{550} for a variety of cases. The dotted lines represent constant ω_{532} values with varying b_{550}. The solid black line uses the fit for the black line in Fig. 17 to calculate ω_{532} from various b_{550}; thus, as the b_{550} increases, this line models the ω_{532} values decreasing as seen by the black line in Fig. 17. The solid red and blue lines in Fig. 18 use the respective limiting trends from Fig. 17 to couple b_{550} and ω_{532}. The limits of the solid lines in Fig. 18 correspond to the end points of the fit lines in Fig. 17. For example, in Fig. 17 the red line ends at b_{550}=0.13 and thus the fit on Fig. 18a does not go past b_{550}=0.13.

The dotted lines in Fig. 18a show that as b_{550} increases, with a constant ω_{532}, the forcing efficiency decreases near-linearly, which indicates an increased cooling of the Earth's surface. Alternatively, as ω_{532} decreases, at a fixed b_{550}, the forcing efficiency increases, indicating increasing warming of the surface. If both b_{550} and ω_{532} are allowed to vary together, a more complex relationship appears. For the red and black line, instead of decreasing the forcing efficiency, the forcing efficiency actually increases with b_{550}, indicating the single scattering albedo dominates the radiative forcing calculation. The blue line still shows decreasing forcing efficiency with increasing b_{550}, but the decrease is not as large as if ω_{532} were held constant.

Figure 18b displays $\Delta F/\delta$ calculated as a function of ω_{532}. The dotted lines show that at a constant b_{550}, the radiative forcing efficiency decreases linearly with increasing

ω_{532}, thus leading to increased cooling potential. The solid red and black lines still have this general trend, but the decrease in forcing efficiency with increasing ω_{532} is diminished, thus the cooling potential of the aerosols is less. It is evident from Fig. 18a and b that for these two cases, ω_{532} has a larger effect on radiative forcing than b_{550}. In contrast, for the upper boundary of the observed ω_{532} vs. b_{550} range (blue line in Figs. 17 and 18), an increase in ω_{532} of 0.90 to 0.97 leads to an increase in radiative forcing efficiency indicating that in this case, changes in b_{550} dominate the changes in overall forcing of the aerosol.

For the type of aerosol present in the PRD region, the expected increase in cooling potential with increasing b_{550} is counteracted by the correlated decrease in the ω_{532}, which results in the aerosols at higher b_{550} having a smaller cooling potential. And the reduction in cooling with decreasing ω_{532} is less than expected because of the increase in b_{550}. This sensitivity test highlights the fact that the coupling of these parameters has the ability to greatly impact radiative forcing and should be considered when modeling the PRD region.

4 Conclusions

The aerosol optical properties at a regional background site in the Pearl River Delta were measured as a part of the PRIDE-PRD2006 campaign. Most of the parameters measured and calculated for this site are similar to those of urban areas, confirming the regional character of air pollution in the PRD. The observed extensive aerosol properties (scattering and absorption coefficients) were much more variable than the derived intensive properties (backscattering fraction, single scattering albedo and Ångström exponent). Both extensive and intensive properties were not greatly influenced by local wind direction, though differences in back trajectories were seen to influence the extensive properties and ω_{532}. A majority of these trajectories (~80%) originated in the heavily populated PRD region (90–180° from the measurement site).

Pronounced diurnal cycles were observed for ω_{532}, $å_s$, σ_s and σ_a. The σ_s and σ_a

ACPD

8, 6845–6901, 2008

values increased at night as the nocturnal boundary layer formed while surface emissions continued, and then decreased during the day due to mixing with the overlying residual layer. The diurnal variation of ω_{532} was also consistent with such mixing and no evidence was found to indicate strong local production of secondary aerosol mass, in spite of a highly photochemically active environment. Only a minor increase in scattering material during the afternoon could be attributed to processes other than mixing. The diurnal cycle of $å_s$ indicates smaller particles in the afternoon, which may be due to new particle formation or temperature-related changes in the gas-particle partitioning of semi-volatile aerosol components.

Low values of single scattering albedos indicate strong emissions of light absorbing carbon, and highly variable ratios of LAC to CO concentration imply a complex mix of combustion sources. Enhanced nighttime levels of LAC appear to be due to diesel soot emissions from regulated truck traffic in the late evening and early morning.

Around periods of intense pollution there was curvature in the dependence of σ_s on wavelength, which caused a wavelength dependence of the Ångström exponent. This curvature can be explained by the high proportion of aerosol volume in the fine fraction.

Single scattering albedo and backscattering fraction exhibited a negative correlation, which can be important for the modeling of the radiative balance in this region.

Acknowledgements. The PRIDE-PRD2006 campaign was sponsored by the China National Basic Research and Development Program (2002CB410801 and 2002CB211605). This study was supported by the Max Planck Society (MPG), the Leibniz Institute for Tropospheric Research (IfT), the University of Tokyo (UT), and Peking University (PKU). Thanks to all team members for support during the campaign and fruitful discussions afterwards, to B. Mamtimin for preparing the population density map and to S. Gunthe for help at the end of the campaign.

References

Adam, M., Pahlow, M., Kovalev, V. A., Ondov, J. M., Parlange, M. B., and Nair, N.: Aerosol optical characterization by nephelometer and lidar: The Baltimore Supersite experiment during the Canadian forest fire smoke intrusion, J. Geophys. Res.-Atmos. 109, D16S02, doi:10.1029/2003JD004047, 2004.

Anderson, T. L., Covert, D. S., Marshall, S. F., Laucks, M. L., Charlson, R. J., Waggoner, A. P., Ogren, J. A., Caldow, R., Holm, R. L., Quant, F. R., Sem, G. J., Wiedensohler, A., Ahlquist, N. A., and Bates, T. S.: Performance characteristics of a high-sensitivity, three-wavelength, total scatter/backscatter nephelometer, J. Atmos. Ocean. Technol., 13(5), 967–986, 1996.

Anderson, T. L., Covert, D. S., Wheeler, J., Harris, J., Perry, K., Trost, B., Jaffe, D., and Ogren, J.: Aerosol backscatter fraction and single scattering albedo: Measured values and uncertainties at a coastal station in the Pacific Northwest, J. Geophys. Res.-Atmos., 104(D21), 26 793–26 807, 1999.

Anderson, T. L., S. J. Masonis, Covert, D. S., Ahlquist, N. C., Howell, S. G., Clarke, A. D., and McNaughton, C. S.: Variability of aerosol optical properties derived from in situ aircraft measurements during ACE-Asia, J. Geophys. Res.-Atmos., 108(D23), 8647, doi:10.1029/2002JD003247, 2003.

Anderson, T. L. and J. A. Ogren: Determining aerosol radiative properties using the TSI 3563 integrating nephelometer, Aerosol Sci. Tech., 29(1), 57–69, 1998.

Andreae, M. O. and A. Gelencser: Black carbon or brown carbon? The nature of light-absorbing carbonaceous aerosols, Atmos. Chem. Phys., 6, 3131–3148, 2006.

Andreae, M. O., Schmid, O., Yang, H., Yu, J.-Z., and Zhang, Y.-H.: Optical properties and chemical composition of the atmospheric aerosol in urban Guangzhou, China, Atmos. Environ., doi:10.1016/j.atmosenv.2008.01.030, 2008.

Andreae, T. W., Andreae, M. O., Ichoku, C., Maenhaut, W., Cafmeyer, J., Karnieli, A., and Orlovsky, L.: Light scattering by dust and anthropogenic aerosol at a remote site in the Negev desert, Israel, J. Geophys. Res.-Atmos., 107(D2), 4008, doi:10.1029/2001JD900252, 2002.

Ångström, A.: On the atmospheric transmission of sun radiation and on dust in the air, Geografiska Annaler, 11, 156–166, 1929.

Arnott, W. P., Moosmuller, H., Rogers, C. F., Jin, T. F., and Bruch, R.: Photoacoustic spectrometer for measuring light absorption by aerosol: instrument description, Atmos. Environ., 33(17), 2845–2852, 1999.

Arnott, W. P., Moosmuller, H., and Walker, J. W.: Nitrogen dioxide and kerosene-flame soot calibration of photoacoustic instruments for measurement of light absorption by aerosols, Rev. Sci. Instrum., 71(12), 4545–4552, 2000.

Ayers, G. P.: Comment on regression analysis of air quality data, Atmos. Environ., 35(13), 2423–2425, 2001.
Baumgardner D., Raga, G., Peralta, O., Rosas, I., Castro, T., Kuhlbusch, T., John, A., and Petzold, A.: Diagnosing black carbon trends in large urban areas using carbon monoxide measurements, J. Geophys. Res., 107(D21), 8342, doi:10.1029/2001JD000626, 2002.
Baumgardner, D.: On the diurnal variability of particle properties related to light absorbing carbon in Mexico City, Atmos. Chem. Phys., 7, 2517–2526, 2007.
Bergin, M. H., Cass, G. R., Xu, J., Fang, C., Zeng, L. M., Yu, T., Salmon, L. G., Kiang, C. S., Tang, X. Y., Zhang, Y. H., and Chameides, W. L.: Aerosol radiative, physical, and chemical properties in Beijing during June 1999, J. Geophys. Res.-Atmos., 106(D16), 17 969–17 980, 2001.
Bond, T. C.: Light absorption by carbonaceous particles: An investigative review, Aerosol Sci. Tech., 40(1), 27–67, 2006.
Bradsher, K.: Trucks power China's economy, at a suffocating cost, The New York Times, NY, 2007.
Cao, J. J., Lee, S. C., Ho, K. F., Zhang, X. Y., Zou, S. C., Fung, K., Chow, J. C., and Watson, J. G: Characteristics of carbonaceous aerosol in Pearl River Delta Region, China during 2001 winter period, Atmos. Environ., 37(11), 1451–1460, 2003.
Cao, J. J., Lee, S. C., Ho, K. F., Zou, S. C., Fung, K., Li, Y., Watson, J. G., and Chow, J. C.: Spatial and seasonal variations of atmospheric organic carbon and elemental carbon in Pearl River Delta Region, China, Atmos. Environ., 38(27), 4447–4456, 2004.
Carrico, C. M., Bergin, M. H. , Xu, J., Baumann, K., and Maring, H.: Urban aerosol radiative properties: Measurements during the 1999 Atlanta Supersite Experiment, J. Geophys. Res.-Atmos., 108(D7), 8422, doi:10.1029/2001JD001222, 2003.
Chen, L. W. A., Doddridge, B. G., Dickerson, R., Chow, J., Mueller, P., Quinn, J., and Butler, W.: Seasonal variations in elemental carbon aerosol, carbon monoxide and sulfur dioxide: Implications for sources, Geophys. Research Lett., 28(9), 1711–1714, 2001.
Cheng, Y., Lee, S. C., Ho, K. F., Wang, Y. Q., Cao, J. J. , Chow, J. C., and Watson, J. G.: Black carbon measurement in a coastal area of south China, J. Geophys. Res.-Atmos., 111, D12310, doi:10.1029/2005JD006663, 2006.
Cheng, Y. F., Eichler, H., Wiedensohler, A., Heintzenberg, J., Zhang, Y. H., Hu, M., Herrmann, H., Zeng, L. M., Liu, S., Gnauk, T., Bruggemann, E., and He, L. Y.: Mixing state of elemental carbon and non-light-absorbing aerosol components derived from in situ particle optical prop-

erties at Xinken in Pearl River Delta of China, J. Geophys. Res.-Atmos. 111(D20), D20204, doi:10.1029/2005JD006929, 2006.

Draxler, R. R. and Rolph, G. D.: HYSPLIT (HYbrid Single-Partilce Lagrangian Integrated Trajectory), available at: http://www.arl.noaa.gov/ready/hysplit4.html, 2003.

Eck, T. F., Holben, B. N., Reid, J., Dubovik, O., Smirnov, A., O'Neill, N., Slutsker, I., and Kinne, S.: Wavelength dependence of the optical depth of biomass burning, urban, and desert dust aerosols, J. Geophys. Res.-Atmos., 104(D24), 31 333–31 349, 1999.

Eck, T. F., B. N. Holben, Ward, D., Dubovik, O., Reid, J., Smirnov, A., Mukelabai, M., Hsu, N., O'Neill, N., and Slutsker, I.: Characterization of the optical properties of biomass burning aerosols in Zambia during the 1997 ZIBBEE field campaign, J. Geophys. Res.-Atmos., 106(D4), 3425–3448, 2001.

Fialho, P., Hansen, A. D. A., and Honrath, R. E.: Absorption coefficients by aerosols in remote areas: a new approach to decouple dust and black carbon absorption coefficients using seven-wavelength Aethalometer data, J. Aerosol Sci., 36(2), 267–282, 2005.

Finlayson-Pitts, B. and Pitts Jr., J.: Chemistry of the Upper and Lower Atmosphere, New York, Academic Press, 1999.

Fujitani, Y., Murao, N., Ohta, S. , Endoh, T., and Yamagata, S.: Optical and chemical properties of marine aerosols over the central equatorial Pacific Ocean during the 2003 R/V Mirai cruise, J. Geophys. Res., 112, (D11213), doi:10.1029/2006JD008354, 2007.

Gobbi, G. P., Kaufman, Y. J., Koren, I., and Eck, T. F.: Classification of aerosol properties derived from AERONET direct sun data, Atmos. Chem. Phys., 7, 453–458, 2007.

Hammer, Ø., Harper, D. A. T., and Ryan, P. D.: PAST: Paleontological Statistics Software Package for Education and Data Analysis, Palaeontol. Electron., 4(1), 1–9, 2001.

Haywood, J. M. and Shine, K. P.: The Effect of Anthropogenic Sulfate and Soot Aerosol on the Clear-Sky Planetary Radiation Budget, Geophys. Research Lett., 22(5), 603–606, 1995.

IPCC: Climate Change 2001: The Scientific Basis, 2001.

Jennings, S. G., Spain, T. G., Doddridge, B., Maring, H., Kelly, B., and Hansen, A.: Concurrent measurements of black carbon aerosol and carbon monoxide at Mace Head, J. Geophys. Res.-Atmos., 101(D14), 19 447–19 454, 1996.

Jiang, M., Marr, L. C., Dunlea, E. J., Herndon, S. C., Jayne, J. T., Kolb, C. E., Knighton, W. B., Rogers, T. M., Zavala, M., Molina, L. T., and Molina, M. J.: Vehicle fleet emissions of black carbon, polycyclic aromatic hydrocarbons, and other pollutants measured by a mobile laboratory in Mexico City, Atmos. Chem. Phys., 5, 3377–3387, 2005.

Kaiser, D. P. and Qian, Y.: Decreasing trends in sunshine duration over China for 1954-1998: Indication of increased haze pollution?, Geophys. Research Lett., 29(21), 2042, doi:10.1029/2002GL016057, 2002.

Keeling, R. F., Piper, S. C., and Heimann, M.: Global and hemispheric CO_2 sinks deduced from changes in atmospheric O_2 concentration, Nature, 381(6579), 218–221, 1996.

Kim, K. W., He, Z. S., and Kim, Y. J.: Physicochemical characteristics and radiative properties of Asian dust particles observed at Kwangju, Korea, during the 2001 ACE-Asia intensive observation period, J. Geophys. Res.-Atmos., 109, D19S02, doi:10.1029/2003JD003693, 2004.

King, M. D. and Byrne, D. M.: Method for Inferring Total Ozone Content from Spectral Variation of Total Optical Depth Obtained with a Solar Radiometer, J. Atmos. Sci., 33(11), 2242–2251, 1976.

Kondo, Y., Komazaki, Y., Miyazaki, Y., Moteki, N., Takegawa, N., Kodama, D., Deguchi, S., Nogami, M., Fukuda, M., Miyakawa, T., Morino, Y., Koike, M., Sakurai, H., and Ehara, K.: Temporal variations of elemental carbon in Tokyo, J. Geophys. Res.-Atmos., 111, D12205, doi:10.1029/2005JD006257, 2006.

Lawrence, M. G., Butler, T. M., Steinkamp, J., Gurjar, B. R., and Lelieveld, J.: Regional pollution potentials of megacities and other major population centers, Atmos. Chem. Phys., 7, 3969–3987, 2007.

Li, C., Marufu, L. T., Dickerson, R. R., Li, Z., Wen, T., Wang, Y., Wang, P., Chen, H., and Stehr, J. W.: In situ measurements of trace gases and aerosol optical properties at a rural site in northern China during East Asian Study of Tropospheric Aerosols: An International Regional Experiment 2005, J. Geophys. Res.-Atmos., 112(D22), D22S04, doi:10.1029/2006JD007592, 2007.

Li, Y., Demetriadesshah, T. H., Kanemasu, E. T., Shultis, J. K., and Kirkham, M. B.: Use of 2nd Derivatives of Canopy Reflectance for Monitoring Prairie Vegetation over Different Soil Backgrounds, Remote Sens. Environ., 44(1), 81–87, 1993.

Lim, H. J.: Origins of primary and secondary organic aerosol in Atlanta: Results' of time-resolved measurements during the Atlanta supersite experiment, Environ. Sci. Technol., 36(21), 4489–4496, 2002.

Liu, S. C., Hu, M., Slanina, S., He, L. Y., Niu, Y., Bruegemann, E., Gnauk, T., and Herrmann, H.: Size distribution of ionic compositions of aerosols in polluted periods at Xinken in Pearl River Delta (PRD) of China, Atmos. Environ., doi:10.1016/j.atmosenv.2007.12.035, 2008.

Malm, W. C., Day, D. E., Carrico, C., Kreidenweis, S. M., Collett Jr., J. L., McMeeking, G., Lee, T., Carrillo, J., and Schichtel, B.: Intercomparison and closure calculations using measurements of aerosol species and optical properties during the Yosemite Aerosol Characterization Study, J. Geophys. Res.-Atmos., 110, D14302, doi:10.1029/2004JD005494, 2005.

Nakajima, T. and A. Higurashi: A use of two-channel radiances for an aerosol characterization from space, Geophys. Res. Lett., 25(20), 3815–3818, 1998.

NBS: National Bureau of Statistics of the People's Republic of China, available at: www.stats.gov.cn, 2007.

Ouyang, T. P., Zhu, Z. Y., and Kuang, Y. Q.: Assessing impact of urbanization on river water quality in the Pearl River Delta Economic Zone, China, Environ. Monit. Assess., 120(1-3), 313–325, 2006.

Park, S. S.: Highly time-resolved organic and elemental carbon measurements at the Baltimore Supersite in 2002, J. Geophys. Res.-Atmos. 110(D7), D07S06, doi:10.1029/2004JD004610, 2005.

Poeschl, U.: Atmospheric aerosols: Composition, transformation, climate and health effects, Angew. Chem. Int. Edit., 44(46), 7520–7540, 2005.

Quinn, P. K. and Bates, T. S.: Regional aerosol properties: Comparisons of boundary layer measurements from ACE 1, ACE 2, aerosols99, INDOEX, ACE asia, TARFOX, and NEAQS, J. Geophys. Res.-Atmos., 110(D14), D14202, doi:10.1029/2004JD004755, 2005.

Quinn, P. K., Coffman, D. J., Kapustin, V. N., Bates, T. S., and Covert, D. S.: Aerosol optical properties in the marine boundary layer during the First Aerosol Characterization Experiment (ACE 1) and the underlying chemical and physical aerosol properties, J. Geophys. Res.-Atmos., 103(D13), 16 547–16 563, 1998.

Quinn, P. K., Coffman, D. J., Bates, T. S., Welton, E. J., Covert, D. S., Miller, T. L., Johnson, J. E., Maria, S., Russell, L., Arimoto, R., Carrico, C. M., Rood, M. J., and Anderson, J.: Aerosol optical properties measured on board the Ronald H. Brown during ACE-Asia as a function of aerosol chemical composition and source region, J. Geophys. Res.-Atmos. 109(D19), D19S01, doi:10.1029/2003JD004010, 2004.

Reid, J. S.: Physical and optical properties of young smoke from individual biomass fires in Brazil, J. Geophys. Res.-Atmos., 103(D24), 32 013–32 030, 1998.

Saathoff, H., Naumann, K. H., Schnaiter, M., Schock, W., Mohler, O., Schurath, U., Weingartner, E., Gysel, M., and Baltensperger, U.: Coating of soot and $(NH_4)(2)SO_4$ particles by ozonolysis products of alpha-pinene, J. Aerosol Sci., 34(10), 1297–1321, 2003.

Schmid, O., Artaxo, P., Arnott, W. P., Chand, D., Gatti, L. V., Frank, G. P., Hoffer, A., Schnaiter, M., and Andreae, M. O.: Spectral light absorption by ambient aerosols influenced by biomass burning in the Amazon Basin. I: Comparison and field calibration of absorption measurement techniques, Atmos. Chem. Phys., 6, 3443–3462, 2006.

Schnaiter, M.: Measurement of wavelength-resolved light absorption by aerosols utilizing a UV-VIS extinction cell, Aerosol Sci. Technol., 39, 249–260, 2005.

Schuster, G. L., Dubovik, O., Holben, B. N.: Angstrom exponent and bimodal aerosol size distributions, J. Geophys. Res.-Atmos., 111, D07207, doi:10.1029/2005JD006328, 2006.

Seinfeld, J. and Pandis, S.: Atmospheric Chemistry and Physics: From Air Pollution to Climate Change, New York, John Wiley & Sons, Inc., 1998.

Sheridan, P. J. and Ogren, J. A.: Observations of the vertical and regional variability of aerosol optical properties over central and eastern North America, J. Geophys. Res.-Atmos., 104(D14), 16 793–16 805, 1999.

Streets, D. G., Bond, T. C., Carmichael, G. R., Fernandes, S. D., Fu, Q., He, D., Klimont, Z., Nelson, S. M., Tsai, N. Y., Wang, M. Q., Woo, J. H., and Yarber, K. F.: An inventory of gaseous and primary aerosol emissions in Asia in the year 2000, J. Geophys. Res.-Atmos. 108(D21), 8809, doi:10.1029/2002JD003093, 2003.

Stunder, B.: available at: http://www.arl.noaa.gov/ready-bin/fnl.pl, 1997.

Takegawa, N., Miyakawa, T., Kondo, Y., Jimenez, J. L., Zhang, Q., Worsnop, D. R., and Fukuda, M.: Seasonal and diurnal variations of submicron organic aerosol in Tokyo observed using the Aerodyne aerosol mass spectrometer, J. Geophys. Res.-Atmos., 111(D11), D11206, doi:10.1029/2005JD006515, 2006.

U.N.: World Urbanization Prospects: The 2005 Revision, available at: http://www.un.org/esa/population/publications/WUP2005/2005WUPHighlights_Final_Report.pdf, 2005.

Waggoner, A. P., Weiss, R. E., Ahlquist, N. C., Covert, D. S., Will, S., and Charlson, R. J.: Optical Characteristics of Atmospheric Aerosols, Atmos. Environ., 15(10-1), 1891–1909, 1981.

Wang, W., M. Rood, Carrico, C. M., Covert, D. S., Quinn, P. K., and Bates, T. S.: Aerosol optical properties along the northeast coast of North America during the New England Air Quality Study-Intercontinental Transport and Chemical Transformation 2004 campaign and the influence of aerosol composition, J. Geophys. Res., 112, D10S23, doi:10.1029/2006JD007579, 2007.

Wei, F., Teng, E., Wu, G., Hu, W., Wilson, W. E., Chapman, R. S., Pau, J. C., and Zhang, J.: Ambient concentrations and elemental compositions of PM_{10} and $PM_{2.5}$ in four Chinese

cities, Environ. Sci. Technol., 33(23), 4188–4193, 1999.
Wiscombe, W. J. and Grams, G. W.: Backscattered Fraction in 2-Stream Approximations, J. Atmos. Sci., 33(12), 2440–2451, 1976.
Wu, D., Tie, X. X., Li, C. C., Ying, Z. M., Lau, A. K. H., Huang, J., Deng, X. J., and Bi, X. Y.: An extremely low visibility event over the Guangzhou region: A case study, Atmos. Environ., 39(35), 6568–6577, 2005.
Xu, J., Bergin, M. H., Yu, X., Liu, G., Zhao, J., Carrico, C. M., and Baumann, K.: Measurement of aerosol chemical, physical and radiative properties in the Yangtze delta region of China, Atmos. Environ., 36(2), 161–173, 2002.

Table 1. Average optical parameters (arithmetic mean ± standard deviation) for the complete campaign, the campaign excluding the "smoky period" (23–25 July) and the "smoky period"; effective limits of detection (ELOD) for the extensive properties.

	All campaign	Campaign without smoky period	Smoky period	ELOD
$\sigma_{s,450}$ (Mm^{-1})	266±271	200±133	791±454	15.6
$\sigma_{bs,450}$ (Mm^{-1})	28.4±25.9	22.4±13.7	76.4±43.7	1.68
$\sigma_{s,550}$ (Mm^{-1})	200±208	151±103	597±358	12.3
$\sigma_{bs,550}$ (Mm^{-1})	23.0±21.6	18.0±11.2	63.0±37.4	1.35
$\sigma_{s,700}$ (Mm^{-1})	137±143	104±72	401±252	8.4
$\sigma_{bs,700}$ (Mm^{-1})	19.9±19.4	15.4±9.7	55.8±34.4	1.20
$\sigma_{a,532}$ (Mm^{-1})	42.5±56.5	34.3±26.5	106±133	5.37
$å_s$ (550/700)	1.57±0.21	1.51±0.22	1.63±0.23	–
$å_s$ (450/700)	1.51±0.20	1.46±0.21	1.50±0.24	–
$å_s$ (450/550)	1.44±0.20	1.38±0.22	1.34±0.25	–
b_{450}	0.11±0.014	0.116±0.013	0.097±0.008	–
b_{550}	0.12±0.016	0.124±0.015	0.106±0.011	–
b_{700}	0.15±0.017	0.154±0.017	0.141±0.014	–
ω_{532}	0.83±0.07	0.82±0.07	0.88±0.06	–

ACPD

8, 6845–6901, 2008

Table 2. Aerosol particle scattering and absorption coefficients, and single scattering albedo values observed in this study and reported for select other campaigns (arithmetic mean ± SD). TSP=total suspended particles.

Location	λ (nm)	σ_s (Mm^{-1})	σ_a (Mm^{-1})	ω	% RH	Inlet	cite
This study	σ_s=550 σ_a=532	151±103	34.3±26.5	0.82±0.07	< 40%	PM_{10}	
Beijing	σ_s=530 σ_a=565	488±370	83±40	0.84±0.08	< 40%	TSP	Bergin et al. (2001)
Xianghe	σ_s=550 σ_a=550	468±472	65±75	0.81–0.85	< 42.5%	TSP	Li et al. (2007)
Guangzhou	σ_s=545 σ_a=532	463±178	92±62	0.839±0.050	< 45%	$PM_{2.5}$	Andreae et al. (2008)
Linan (Yangtze delta)	σ_s=530 σ_a=565	353±202	23±14	0.93±0.04	< 40%	$PM_{2.5}$	Xu et al. (2002)
Ace-Asia (Dust-Frontal)	σ_s=550 σ_a=550	330±31	14±7.0	0.96±0.02	55%	PM_{10}	Quinn et al. (2004)
Kwangju, Korea	σ_s=520 σ_a=880	319±222	42±12	0.84–0.93	ambient	PM_{10}	Kim et al. (2004)
Xinken (PRD)	σ_s=550 σ_a=630	301±125	61±37		< 20%	PM_{10}	Cheng et al. (2006)
Ace-Asia (Dust + Shanghai)	σ_s=550 σ_a=550	202±63	17±6.5		55%	PM_{10}	Quinn et al. (2004)
Ace-Asia (volcano + polluted)	σ_s=550 σ_a=550	188±67	9.0±3.0		55%	PM_{10}	Quinn et al. (2004)
Baltimore, USA (smoke)	σ_s=530	126±80			ambient	TSP	Adam et al. (2004)
Atlanta	σ_s=530 σ_a=550	121±48	16±12	0.87±0.08	48±5%	$PM_{2.5}$	Carrico et al. (2003)
Ace-Asia (Dust + Korea)	σ_s=550 σ_a=550	120±57	8.4±2.5		55%	PM_{10}	Quinn et al. (2004)
Ace-Asia (polluted-Japan)	σ_s=550 σ_a=550	114±16	11±2.	0.91±0.01	55%	PM_{10}	Quinn et al. (2004)
Negev Desert, Israel	σ_s=550	86.7±53.8			ambient	TSP	Andreae et al. (2002)
Ace-Asia (airborne)	σ_s=550 σ_a=550	83.3±100.6	7±8.3	0.923±0.032	< 40%	TSP	Anderson et al. (2003)
Ace-Asia (polluted-Korea/Japan)	σ_s=550 σ_a=550	69±11	7.9±1.5		55%	PM_{10}	Quinn et al. (2004)
NEAQS-ITCT (NE US)	σ_s=550	42.9±35.2		0.92±0.06	26±4%	PM_1	Wang et al. (2007)
Yosemite Valey, USA	σ_s=530	37.28±28.99			"dry"	PM_{10}	Malm et al. (2005)
Baltimore, USA (pre-smoke)	σ_s=530	32±19			ambient	TSP	Adam et al. (2004)
Ace-Asia (marine)	σ_s=550 σ_a=550	29±17	0.79±0.71	0.97±0.03	55%	PM_{10}	Quinn et al. (2004)
ACE1	σ_s=550	23±16		0.9	30–45%	1 μm–10 μm	Quinn et al. (1998)
Pacific NW, USA (North America Continental)	σ_s=550 σ_a=550	10.79±5.33	1.39±0.54	0.886±0.031	< 40%	PM_1	Anderson et al. (1999)
Pacific NW, USA (Asian modified marine)	σ_s=550 σ_a=550	8.57±6.27	0.08±0.12	0.909±0.007	< 40%	PM_1	Anderson et al. (1999)
Pacific NW, USA (North America modified marine)	σ_s=550 σ_a=550	6.49±5.31	0.80±0.98	0.895±0.059	< 40%	PM_1	Anderson et al. (1999)
Baltimore, USA (post-smoke)	σ_s=530	6±3			ambient	TSP	Adam et al. (2004)
ACE1	σ_s=550	4.4±3			30–45%	PM_1	Quinn et al. (1998)
Pacific NW, USA (Marine)	σ_s=550 σ_a=550	3.34±2.31	0.09±0.13	0.974±0.034	< 40%	PM_1	Anderson et al. (1999)
Equatorial Pacific Ocean	σ_s=530 σ_a=565	3.2±2.41	0.6±0.05	0.976±0.01	65±4%	PM_2	Fujitani et al. (2007)

Table 3. Extensive and intensive aerosol optical properties (daily mean ± SD) for the days highlighted in Fig. 11. The "Back Trajectories" column provides a short description for this day's air mass.

Date	Back Trajectories	$\sigma_{s,550}$ (Mm^{-1})	$\sigma_{a,532}$ (Mm^{-1})	$å_s$ (450/700)	b_{550}	ϖ_{532}
12 July 2006	Local from S, re-circulating,	297±90	53.8±42.3	1.42±0.15	0.107±0.006	0.871±0.066
13 July 2006	Continental, from W/NW	263±203	52.9±49.5	1.41±0.14	0.101±0.005	0.846±0.055
20 July 2006	Slow, from SW	228±84	41.2±25.6	1.65±0.27	0.130±0.013	0.868±0.048
21 July 2006	Slow, from S/SW	201±112	43.6±30.1	1.63±0.25	0.143±0.019	0.846±0.040
10 July 2006	SE, large rain event (start 13:15)	177±106	50.7±40.7	1.44±0.21	0.125±0.012	0.786±0.065
18 July 2006	Marine, SE over PRD	114±26	25.8±11.1	1.37±0.22	0.126±0.006	0.825±0.052
4 July 2006	Marine, Fast SE over PRD	96.7±31.8	34.3±15.4	1.44±0.21	0.139±0.008	0.750±0.054
3 July 2006	Marine, SE over PRD	88.7±34.8	31.0±16.7	1.42±0.19	0.141±0.010	0.761±0.051
28 July 2006	Marine, from E	86.5±40.3	21.8±8.7	1.60±0.15	0.126±0.013	0.806±0.048

ACPD
8, 6845–6901, 2008

Aerosol optical properties near Guangzhou

R. M. Garland et al.

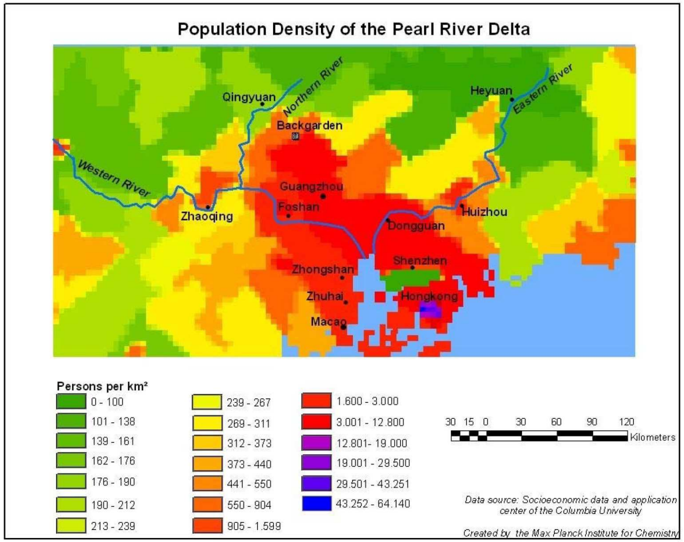

Fig. 1. Map of southeastern China colored by population density. The measurement location (Backgarden) and major cities in the area are labeled.

ACPD

8, 6845–6901, 2008

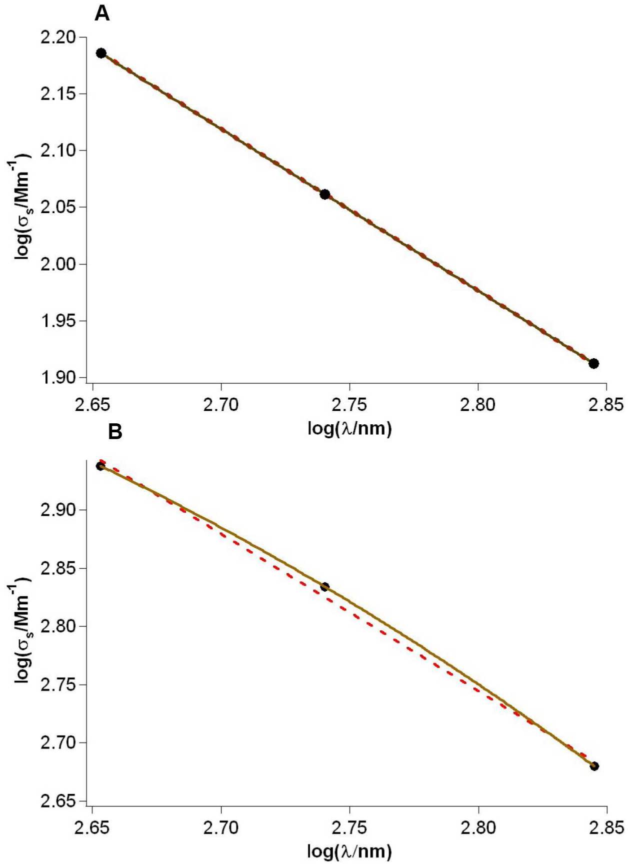

Fig. 2. Double-logarithmic plot of scattering coefficient (σ_s) versus wavelength (λ) for **(A)** 18 July 2006 and **(B)** 25 July 2006. The dotted line is a linear fit. The negative slope of this fit is the Ångström exponent ($å_s$). The solid line is a second order polynomial fit (King and Byrne 1976).

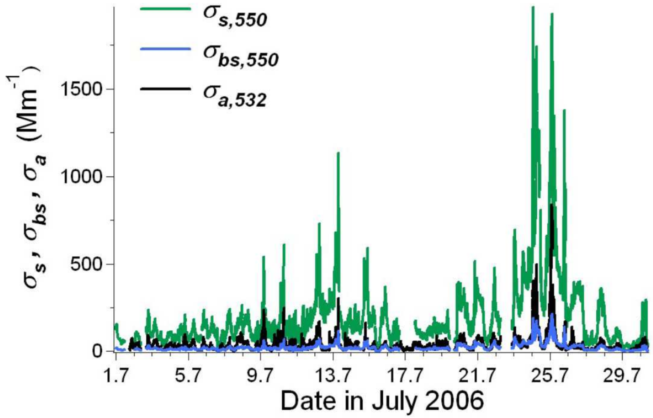

Fig. 3. Time series for the extensive optical properties measured in the green spectral range: scattering, backscattering, and absorption coefficients ($\sigma_{s,550}$, $\sigma_{bs,550}$, $\sigma_{a,532}$).

ACPD
8, 6845–6901, 2008

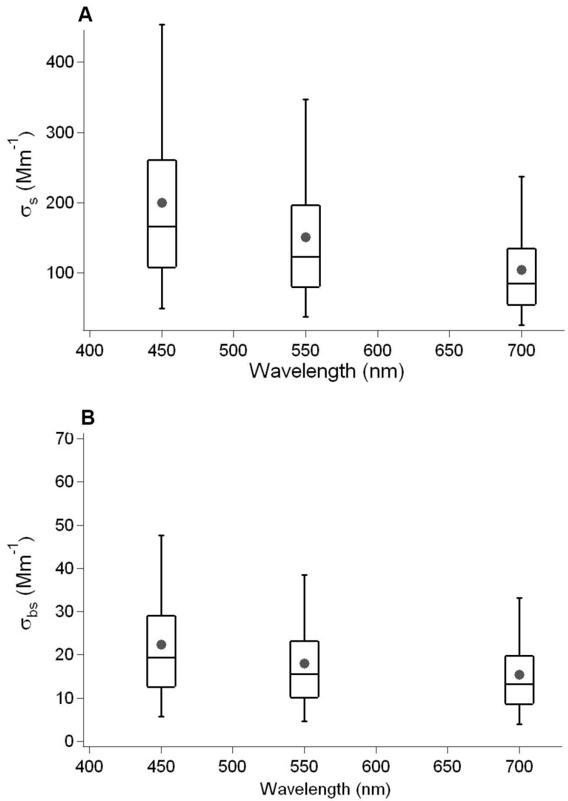

Fig. 4. Statistical distribution of **(A)** scattering coefficients (σ_s) and **(B)** backscattering coefficients (σ_{bs}) measured with the three-wavelength nephelometer for the campaign (excluding 23–25 July). The dot is the mean value, the horizontal line in the box is the median, the limits of the boxes are the 25% and 75% and the vertical lines extend to 5% and 95%.

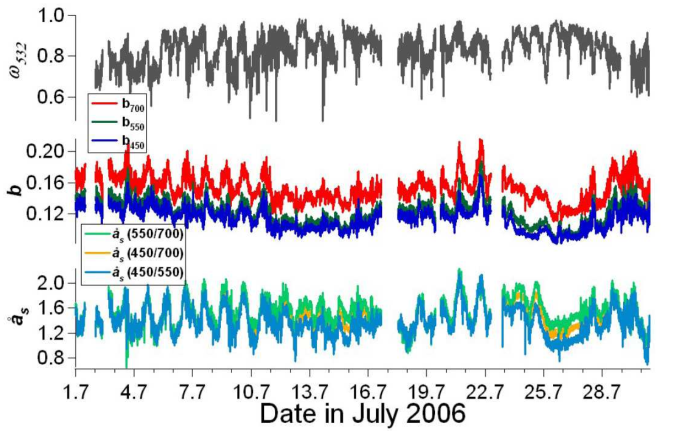

Fig. 5. Time series for the intensive optical properties: single scattering albedo (ω_{532}), backscattering fraction (b) and Ångström exponent ($å_s$).

ACPD
8, 6845–6901, 2008

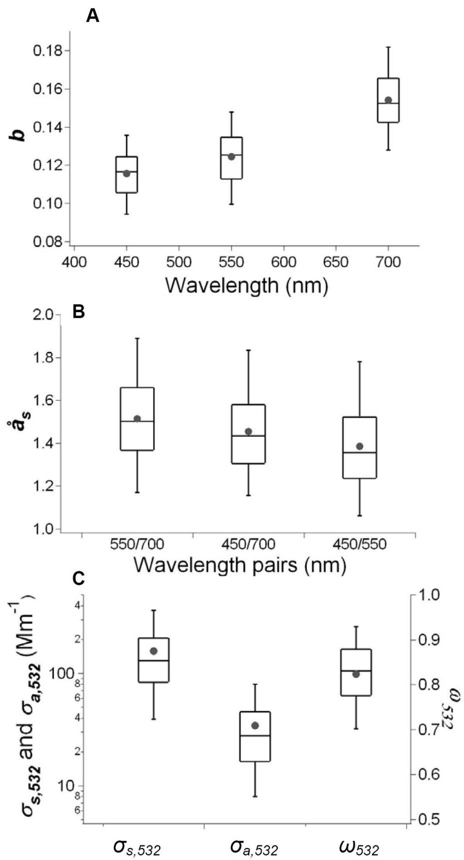

Fig. 6. Statistical distribution of **(A)** backscattering fraction (b) for different wavelengths, **(B)** Ångström exponent ($å_s$) for different wavelength pairs, and **(C)** scattering and absorption coefficient and single scattering albedo at 532 nm ($\sigma_{s,532}$, $\sigma_{a,532}$, ϖ_{532}) for the campaign (excluding 23–25 July).

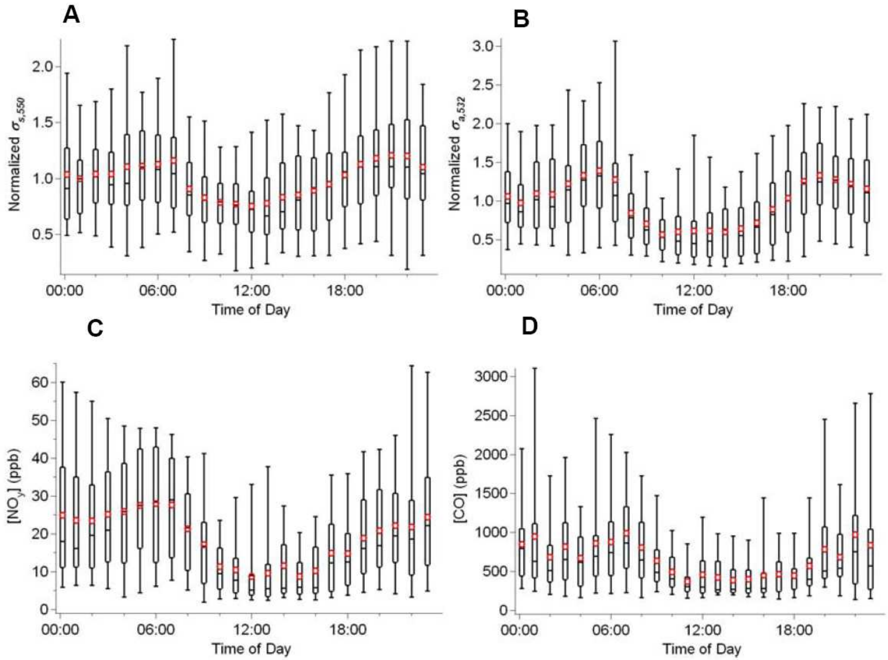

Fig. 7. Diurnal variations of **(A)** normalized $\sigma_{s,550}$, **(B)** normalized $\sigma_{a,532}$, **(C)** $[NO_y]$ and **(D)** [CO] averaged over the campaign (excluding 23–25 July).

ACPD
8, 6845–6901, 2008

Aerosol optical properties near Guangzhou

R. M. Garland et al.

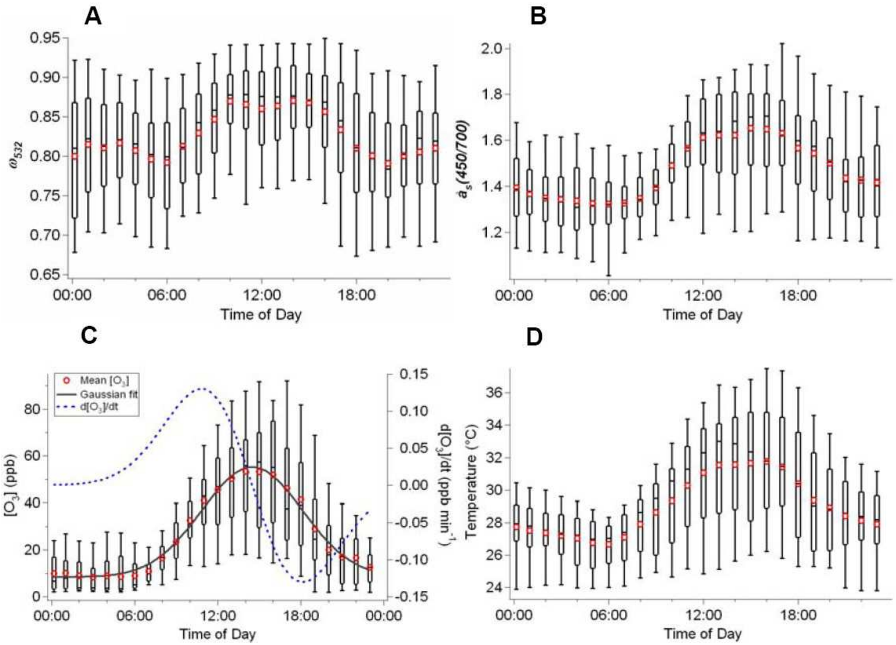

Fig. 8. Diurnal variations of **(A)** ω_{532}, **(B)** $å_s$ (450/700), **(C)** $[O_3]$ and $d[O_3]/dt$ and **(D)** ambient temperature averaged over the campaign (excluding 23–25 July).

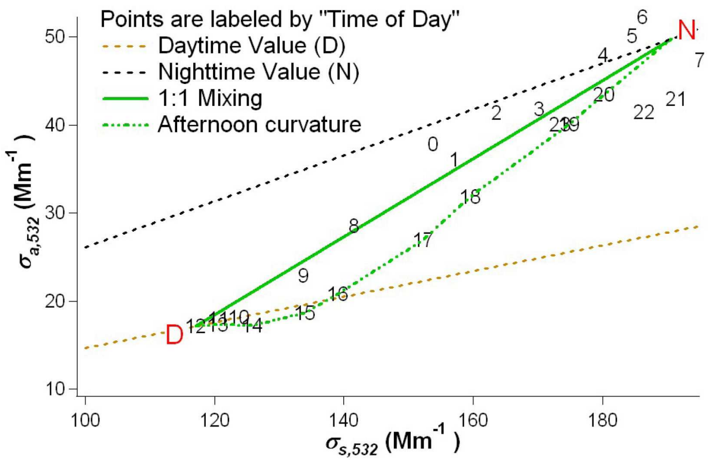

Fig. 9. Mixing diagram for $\sigma_{a,532}$ and $\sigma_{s,532}$ relationship. The characteristic day ratio (point D) is 12:00 and the characteristic night value is between 6:00 and 7:00 (point N). The black and brown dotted lines are fit through each of these points and zero. The solid green line represents the 1:1 mixing of "D" and "N" values. The dotted green line highlights the curvature seen in afternoon. Data points are arithmetic mean values averaged over the campaign (excluding 23–25 July).

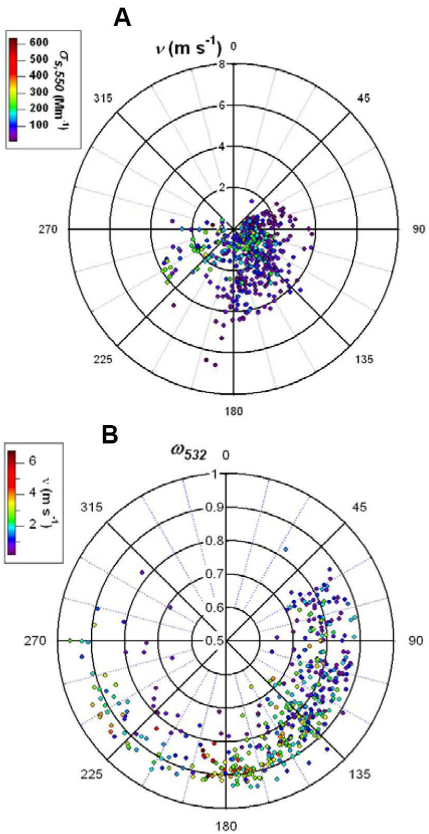

Fig. 10. Local wind direction and wind speed plots for the campaign (excluding 23–25 July): **(A)** wind direction versus wind speed (m s^{-1}) with the color scale as $\sigma_{s,550}$ (Mm^{-1}) and **(B)** wind direction versus ω_{532} with wind speed (m s^{-1}) as the color scale.

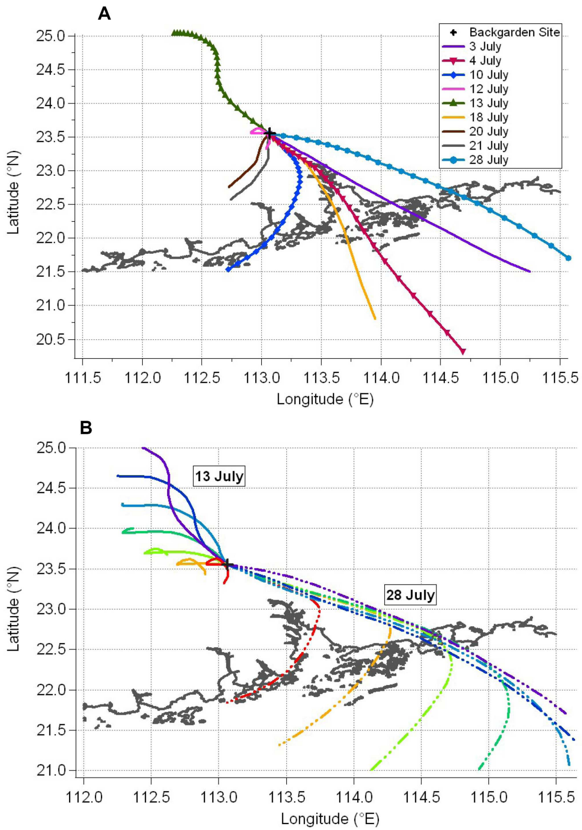

Fig. 11. Hysplit 24-h back trajectories for **(A)** all highlighted days (start time 24:00); **(B)** 13 July, solid lines, and 28 July, dotted lines, start times are purple=24:00, dark blue=20:00, light blue=16:00, green=12:00, light green=8:00, orange=4:00, red=0:00). All times refer to local time and all trajectories had an initial elevation of 100 m.

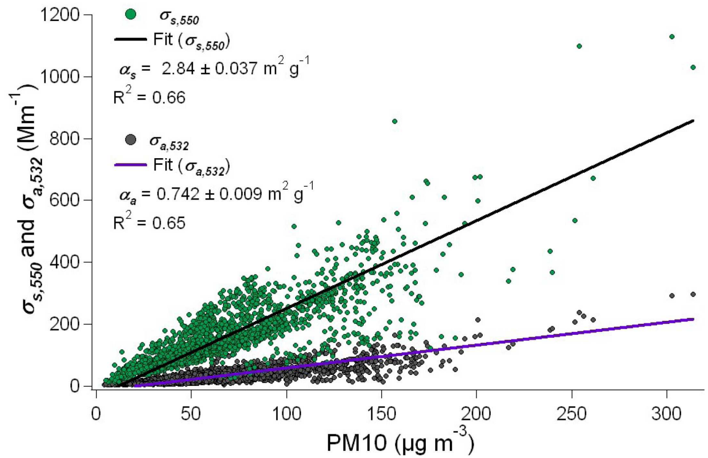

Fig. 12. $\sigma_{s,550}$ and $\sigma_{a,532}$ vs. PM_{10} mass (dry particles) for the campaign (excluding 23–25 July). The lines are the reduced major axis best fit. The slope of the lines are the mass scattering efficiency ($\alpha_{s,550}$) and mass absorption efficiency ($\alpha_{a,532}$).

ACPD
8, 6845–6901, 2008

Title Page
Abstract
Introduction
Conclusions
References
Tables
Figures
◂
▸
Back
Close
Full Screen / Esc
Printer-friendly Version
Interactive Discussion

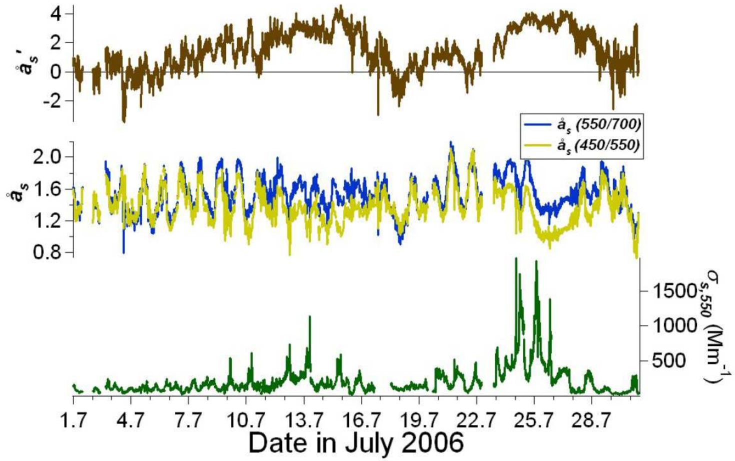

Fig. 13. Time series for second derivative ($å_s'$), Ångström exponent ($å_s$) and total scattering coefficient ($\sigma_{s,550}$).

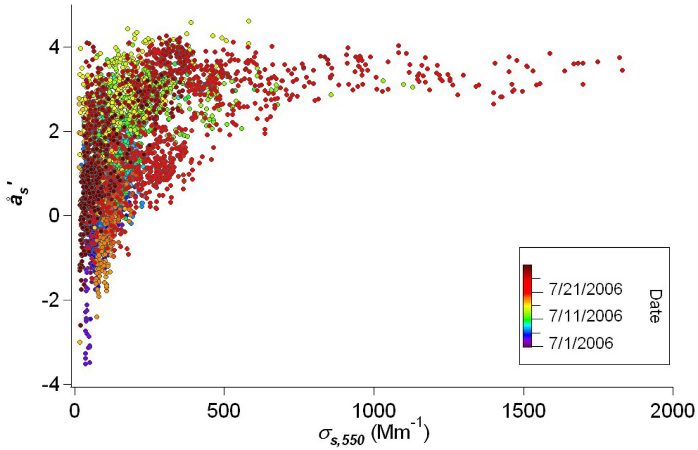

Fig. 14. Second derivative ($\mathring{a}_s'$) versus scattering coefficient ($\sigma_{s,550}$) for the whole campaign, including 23–25 July.

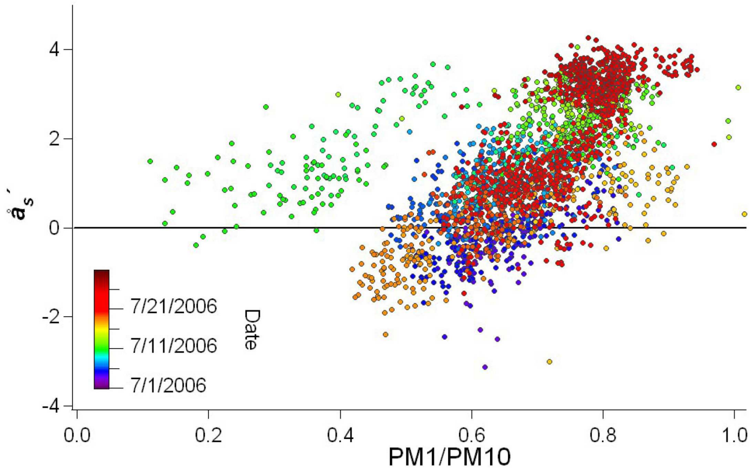

Fig. 15. Second derivative ($\mathring{a}_s'$) versus PM_1/PM_{10} for the whole campaign, including 23–25 July.

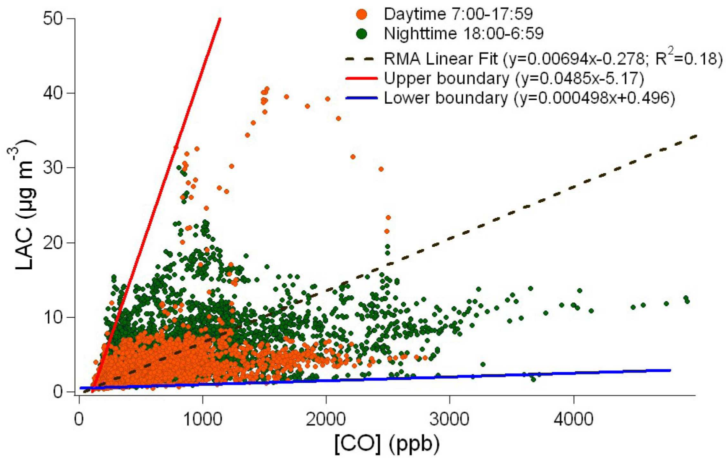

Fig. 16. Light absorbing carbon (LAC) mass concentration versus carbon monoxide mixing ratio. The dotted line is the reduced major axis best fit and the solid lines are boundary conditions.

ACPD
8, 6845–6901, 2008

Title Page
Abstract | Introduction
Conclusions | References
Tables | Figures
◀I | ▶I
◀ | ▶
Back | Close
Full Screen / Esc
Printer-friendly Version
Interactive Discussion

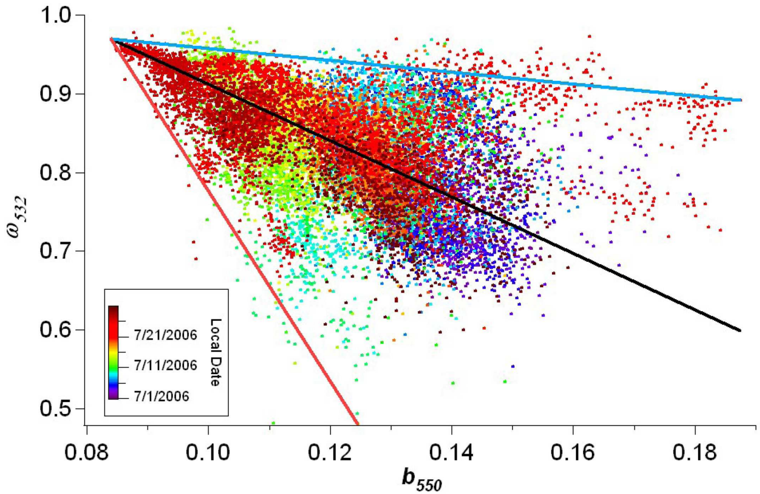

Fig. 17. Single scattering albedo (532 nm) versus backscattering fraction (550 nm) for the whole campaign, including 23–25 July. The black line is a linear fit and the red and blue lines represent lower and upper boundaries, respectively.

ACPD

8, 6845–6901, 2008

Aerosol optical properties near Guangzhou

R. M. Garland et al.

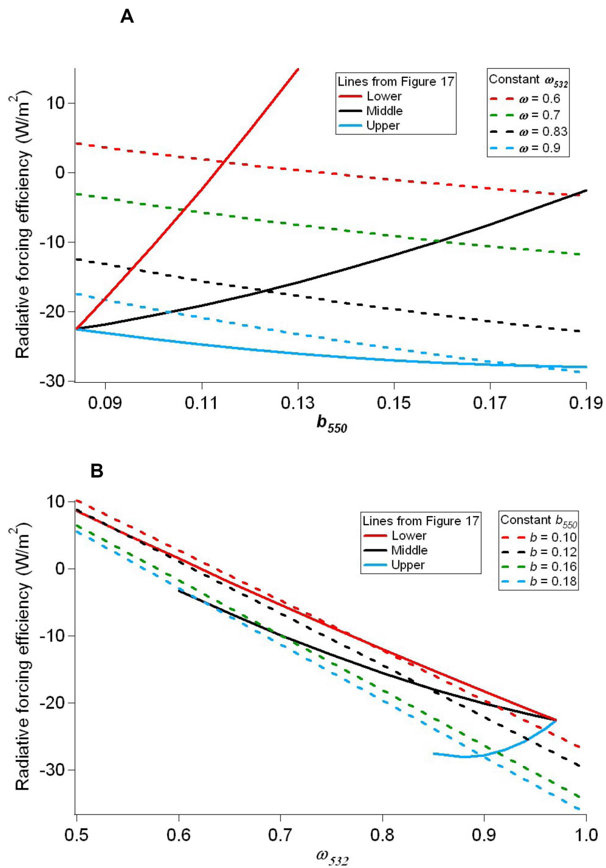

Fig. 18. **(A)** Radiative forcing efficiency calculated from Eq. (6) as a function of b_{550}. The dotted lines are assuming a constant ω_{532} value. **(B)** Radiative forcing efficiency from Eq. (6) as a function of ω_{532}. The dotted lines assume a constant b_{550}. For both graphs the solid line calculates the ω_{532} values from the b_{550} using the fit displayed in Fig. 17.